Bulletin of the Seismological Society of America, Vol. XX, No. XX, pp. –, – 2018, doi: 10.1785/0120170179

Ground-Motion Prediction Equations for Central and Eastern North America Using the Hybrid Empirical Method and NGA-West2 Empirical Ground-Motion Models

by Shahram Pezeshk, Arash Zandieh, Kenneth W. Campbell, and Behrooz Tavakoli

Abstract The hybrid empirical method (HEM) of simulating ground-motion intensity measures (GMIMs) in a target region uses stochastically simulated GMIMs in the host and target regions to develop adjustment factors that are applied to empirical GMIM predictions in the host region. In this study, the HEM approach was used to develop two new ground-motion prediction equations (GMPEs) for a target region defined as central and eastern North America (CENA), excluding the Gulf Coast region. The method uses five new empirical GMPEs developed by the Pacific Earthquake Engineering Research Center for the Next Generation Attenuation-West2 (NGA-West2) project to estimate GMIMs in the host region. The two new CENA GMPEs are derived for peak ground acceleration and response spectral ordinates at periods ranging from 0.01 to 10 s, moment magnitudes (**M**) ranging from 4.0 to 8.0, and rupture distance (R_{rup}) as far as 1000 km from the site, although the GMPEs are best constrained for $R_{\mathrm{rup}} < 300$–400 km. The predicted GMIMs are for a reference site defined as CENA hard rock with $V_{S30} = 3000$ m/s and $\kappa_0 = 0.006$ s.

The seismological parameters for the western North America host region were adopted from a point-source inversion of the median GMIM predictions from the NGA-West2 GMPEs for events and sites with $\mathbf{M} \le 6.0$, $R_{\mathrm{rup}} \le 200$ km, $V_{S30} = 760$ m/s, a generic (average of strike slip and reverse) style of faulting, and earthquake-depth and sediment-depth parameters equal to the default values recommended by the NGA-West2 developers. The two CENA GMPEs are based on two fundamentally different approaches to magnitude scaling at large magnitudes: (1) using the HEM approach to model magnitude scaling over the entire magnitude range and (2) using the HEM approach to model magnitude scaling for events with $\mathbf{M} \le 6.0$ and using the magnitude scaling predicted by the NGA-West2 GMPEs for the larger events.

Introduction

For seismic hazard applications, ground-motion amplitudes are often estimated using ground-motion prediction equations (GMPEs). GMPEs relate ground-motion intensity measures (GMIMs), such as peak ground acceleration (PGA), peak ground velocity, and 5% damped pseudoacceleration linear-elastic response spectral acceleration (PSA), to seismological parameters in a specified region, such as earthquake magnitude, source-to-site distance, local site conditions, and style of faulting. In areas of the world where ground-motion recordings are plentiful because of their active seismicity and tectonics and the presence of a dense instrumental recording network (e.g., western North America [WNA]), the GMPEs are empirically obtained from a statistical regression of the ground-motion recordings (Douglas, 2003, 2011). An example of such empirical GMPEs are those developed as part of the Next Generation Attenuation Phase 2 (NGA-West2) project (Bozorgnia *et al.*, 2014) conducted by the Pacific Earthquake Engineering Research Center (PEER). Five individual GMPEs were developed for WNA and other active tectonic regions in the world as part of the NGA-West2 project (Abrahamson *et al.*, 2014; Boore *et al.*, 2014; Campbell and Bozorgnia, 2014; Chiou and Youngs, 2014; Idriss, 2014) and are compared by Gregor *et al.* (2014).

Empirical methods cannot be used to develop GMPEs that are valid for moderate to large magnitudes for regions with limited strong ground motion data. Central and eastern North America (CENA) is an example of such a region, which is considered to be a stable continental regime with abundant recordings of ground motion from distant small and moderate events but with limited ground-motion recordings from the near-source region and from large-magnitude earthquakes of greatest engineering interest. In areas such as CENA, stochastic methods (e.g., Boore, 2003) are valuable and are often used as simple methods to estimate ground motions for the distance and magnitude range of engineering interest. Stochastic ground-motion simulations are used to develop GMPEs using the same empirical regression approach that is applied to recorded ground-motion data. In the simplest application of the stochastic simulation approach, a stochastic point-source method is used as a framework to estimate a ground-motion time series and related GMIMs using simple seismological models of the source spectrum (Brune, 1970, 1971), wave-propagation path, and local site conditions (McGuire and Hanks, 1980; Hanks and McGuire, 1981; Boore 1983, 2003, 2005). Atkinson and Boore (1995, 1998), Frankel *et al.* (1996), Toro *et al.* (1997), Silva *et al.* (2002), and Pezeshk *et al.* (2015) provide examples of GMPEs developed for CENA using the point-source stochastic method. Boore (2015) used five models (Atkinson and Boore, 1995, 2014; Silva *et al.*, 2002; Boore *et al.*, 2010; Boatwright and Seekins, 2011) for point-source stochastic-method simulations for the PEER NGA-East project. The method was extended to include finite-fault effects by Silva *et al.* (1990), Beresnev and Atkinson (1997, 1998, 1999, 2002), Motazedian and Atkinson (2005), and Boore (2009). Atkinson and Boore (2006, 2011) give examples of GMPEs developed for CENA using the finite-fault stochastic method.

GMPEs developed from empirical data are often well constrained, depending on the completeness of the database, and represent the inherent characteristics of ground-motion scaling in the near-source region of large earthquakes. On the other hand, GMPEs obtained from stochastic point-source models may lack realistic near-source characteristics, especially magnitude-scaling effects as saturation of ground motion with increasing magnitude and decreasing distance, because of the assumption that the total seismic energy is released from a single point within the crust. Modeling of this magnitude–distance saturation effect in point-source stochastic models can be improved through the use of a double-corner-frequency source spectrum (Atkinson and Boore, 1995, 1998; Atkinson and Silva, 1997), an effective point-source distance metric (Atkinson and Silva, 2000; Boore, 2009; Yenier and Atkinson, 2014), stochastic finite-fault models (see above references), well-calibrated physics-based models (Somerville *et al.*, 2001, 2009; Dreger *et al.*, 2015), or the hybrid empirical modeling method (Campbell, 2003, 2014).

In this study, we use the hybrid empirical method (HEM) to develop GMPEs for use in CENA as part of the NGA-East project (Goulet *et al.*, 2014; see Data and Resources). The HEM approach is a well-accepted procedure to develop GMPEs in areas with limited ground-motion recordings. In the HEM approach, GMIMs in a target region (CENA in this study) are predicted from empirical GMPEs in a host region (WNA in this study) using seismological-based adjustment factors between the two regions. The adjustment factors are calculated as the ratio of stochastically simulated GMIMs in the two regions. Using appropriate regional seismological parameters in the stochastic simulations, the calculated adjustment factors take into account differences in earthquake source, wave propagation, and site-response characteristics between the two regions. The empirically derived GMPEs for the host region are transferred to the target region by applying the regional adjustment factors to the empirical GMIM predictions from which a GMPE is derived using standard regression analysis. The HEM approach has been used by several researchers to develop GMPEs in CENA (Campbell, 2003, 2007, 2008, 2011; Tavakoli and Pezeshk, 2005; Pezeshk *et al.*, 2011, 2015; Shahjouei and Pezeshk, 2016), in central Europe (Scherbaum *et al.*, 2005), and in southern Spain and southern Norway (Douglas *et al.*, 2006). Campbell (2014) provides a complete review of these and other applications of the HEM approach.

Campbell (2003) developed a HEM-based GMPE for CENA hard-rock site conditions using contemporary stochastic point-source models and four pre-NGA WNA empirical GMPEs. Campbell (2007) updated this GMPE for National Earthquake Hazards Reduction Program (NEHRP) B/C site conditions using CENA seismological parameters recommended by Atkinson and Boore (2006) and the NGA-West1 empirical GMPE developed for WNA by Campbell and Bozorgnia (2008). Campbell (2008, 2011) extended the model developed by Campbell (2007) to CENA hard-rock site conditions by including an empirical hard-rock amplification model developed by Atkinson and Boore (2006). During that process, he discovered that a relatively high stress parameter ($\Delta\sigma$) of 280 bars was needed to force agreement between the point-source simulations that he did and finite-fault stochastic simulations of Atkinson and Boore (2006), which had used a stress parameter of 140 bars. This apparent discrepancy was later explained by Atkinson *et al.* (2009) and Boore (2009). Tavakoli and Pezeshk (2005) proposed a HEM-based model for CENA hard-rock site conditions that used a magnitude-dependent stress parameter in the WNA stochastic GMIM simulations. They used a generic source function that combined single-corner and double-corner source-spectrum models and an effective point-source distance metric, based on the effective-depth model proposed by Atkinson and Silva (2000), to force the stochastic point-source model to mimic finite-fault effects and to account for magnitude–distance saturation effects. Pezeshk *et al.* (2011) updated Tavakoli and Pezeshk (2005) using the Atkinson and Boore (2006) CENA seismological parameters with a stress parameter of 250 bars in the stochastic GMIM simulations to obtain better agreement with the Atkinson and Boore (2006) finite-fault simulations. The use of a 250-bar rather than a 140-bar stress parameter with the point-source stochastic simulations was recommended by Atkinson *et al.* (2009) and Boore (2009). Pezeshk *et al.* (2011) derived their HEM-based GMPE for CENA hard-rock site conditions using the empirical crustal-amplification factors proposed by Atkinson and Boore (2006) and adopted an effective point-source distance metric to mimic finite-fault effects.

The purpose of this study is to update the HEM-based GMPES of Campbell (2007, 2008, 2011) and Pezeshk *et al.* (2011, 2015) for CENA using the five new empirical GMPEs developed in the PEER NGA-West2 project (Bozorgnia *et al.*, 2014) for WNA and other shallow crustal active tectonic r egions (Abrahamson *et al.*, 2014; Boore *et al.*, 2014; Campbell and Bozorgnia, 2014; Chiou and Youngs, 2014; Idriss, 2014) and the latest information on CENA seismological parameters (Chapman *et al.*, 2014; Hashash, Kottke, Stewart, Campbell, Kim, Moss, *et al.*, 2014; Boore and Thompson, 2015; Yenier and Atkinson, 2015a). Although we use stochastic point-source models for both CENA and WNA to obtain simulated GMIMs for the development of regional adjustment factors, we limit their use to $\mathbf{M} \le 6.0$ to avoid the need to explicitly include finite-fault effects and to stay within the magnitude range of data used to develop the CENA stochastic model used in this study and the NGA-East database (Goulet *et al.*, 2014; see Data and Resources). A horizontal-component GMPE functional form similar to that in Pezeshk *et al.* (2011) is used to develop the GMPEs, and a nonlinear regression analysis is performed to estimate period-dependent model coefficients for **M** 4.0–8.0 and $R_{\mathrm{rup}} \le 1000$ km. GMPEs are developed for PGA and 5% damped PSA for CENA reference hard-rock site conditions recommended by Hashash, Kottke, Stewart, Campbell, Kim, Moss, *et al.* (2014). The GMIM predictions are extended to $\mathbf{M} > 6.0$ using two different methods. We compare the GMIM predictions from our two new GMPEs with our previous GMPEs as well as with observed GMIMs from the available NGA-East database.

Stochastic Ground-Motion Simulation

We developed a set of computer routines based on the random vibration method of Kottke and Rathje (2008) to perform the point-source stochastic simulation of GMIM amplitudes using the WNA and CENA seismological models. The output of the program is PGA and PSA at a preselected set of spectral periods (T). The regional adjustment factors are the ratio of the simulated spectral values for CENA with respect to those for WNA. In the stochastic method, the ground-motion acceleration is modeled as filtered Gaussian white noise modulated by a deterministic envelope function defined by a specified set of seismological parameters (Boore, 2003). The filter parameters are determined by either matching the properties of an empirically defined spectrum of strong ground motion with theoretical spectral shapes or using reliable physical characteristics of the earthquake source and propagation media (Hanks and McGuire, 1981; Boore, 1983, 2003). Atkinson *et al.* (2009) and Boore (2009) investigated the relationship between the stochastic point-source model Stochastic-Method SIMulation (SMSIM; Boore, 2005) and the stochastic finite-fault model EXSIM (Motazedian and Atkinson, 2005) and suggested how the two could be aligned to give better agreement in predicted motions from small earthquakes at large distances, where the two models should provide similar results.

In the point-source model, the total Fourier amplitude spectrum (FAS) of the horizontal vibratory ground displacement $Y(M_0, R, f)$ due to shear-wave propagation can be modeled by the equation:

$$Y(M_0, R, f) = S(M_0, f)P(R, f)G(f)I(f) \qquad (1)$$

(Boore, 2003), in which M_0 is seismic moment (dyn · cm), R is source-to-site distance (km), f is frequency (Hz), $S(M_0, f)$ is the source spectrum, $P(R, f)$ is the path attenuation term, $G(f)$ is the site-response term, and $I(f)$ is a filter representing the type of GMIM. The FAS of acceleration is obtained by multiplying $Y(M_0, R, f)$ by ω^2.

Effective Point-Source Distance

In the stochastic point-source model, the earthquake source is assumed to be concentrated at a point within the crust, which is a reasonable assumption for small earthquakes or when the source-to-site distance is considerably larger than the earthquake source dimensions. Otherwise, empirical and physics-based models show that finite-fault effects in the form of magnitude and distance saturation begin to influence the ground motions. This reflects the fact that seismic waves with wavelengths much smaller than the earthquake source-rupture dimensions do not increase in amplitude as the size of the earthquake and the corresponding energy release increase (Tavakoli and Pezeshk, 2005; Yenier and Atkinson, 2014). It has also been suggested that when source fault-rupture lengths are much larger than the closest distance to the rupture surface, the motions recorded at this close station will only have contributions from the closest part of the rupture, with the energy from greater distances along the fault arriving in a more attenuated form (e.g., Boore and Thompson, 2014; Baltay and Hanks, 2014).

Atkinson and Silva (2000) defined an effective point-source distance metric R'_{rup} to use in point-source stochastic simulations to mimic the ground-motion saturation effects from finite-fault effects. They also defined a magnitude-dependent equivalent point-source depth $h(\mathbf{M})$ to modify this distance for magnitude-saturation effects. Following these authors, we define an effective point-source distance metric to use with our point-source stochastic simulations with the expression:

$$R'_{\mathrm{rup}} = \sqrt{R_{\mathrm{rup}}^2 + h(\mathbf{M})^2}, \qquad (2)$$

in which the pseudodepth $h(\mathbf{M})$, also referred to as the finite-fault factor by Boore and Thompson (2014), is defined by the expression:

$$\log(h(\mathbf{M})) = \begin{cases} \max(-0.05 + 0.15\mathbf{M}, -1.72 + 0.43\mathbf{M}) & \mathbf{M} \le 6.75 \\ -0.405 + 0.235\mathbf{M} & \mathbf{M} > 6.75 \end{cases}, \quad (3)$$

which combines the pseudodepth relationships developed by Atkinson and Silva (2000) and Yenier and Atkinson (2014, 2015a,b) to provide a consistent set of effective distances over the entire magnitude range of interest.

We use the effective point-source distance metric in the stochastic simulations to evaluate the adjustment factors for a given set of magnitude and distances. This is done by (1) evaluating the NGA-West2 GMPEs for a given set of $\mathbf{M}$ and R_{rup} values, (2) calculating the corresponding values of R'_{rup} from equations (2) and (3), (3) using the values of R'_{rup} to determine the stochastic adjustment factors, and (4) using the adjustment factors to derive the HEM-based GMIM estimates for the original set of $\mathbf{M}$ and R_{rup} values.

Site Response

The site-response term $G(f)$ is defined as the product of crustal-amplification and diminution functions (Boore, 2003). Crustal amplification is calculated using the quarter-wavelength (QWL) method, which Boore (2013) now refers to as the square-root-impedance (SRI) method. Boore (2003) proposes the maximum frequency filter $f_{\max}$ (Hanks, 1982) and the kappa filter κ_0 (Anderson and Hough, 1984) as alternatives to model the site diminution function. The kappa filter $\exp(-\pi\kappa_0 f)$ can be considered the path-independent loss of energy in the ground motion as it propagates through the site profile. It is defined empirically by Anderson and Hough (1984) as the high-frequency slope of the FAS on a log–linear plot. Although kappa can be calculated from a recording at any distance, the part of kappa that is associated with the crustal profile beneath the site κ_0 includes attenuation from both wave scattering and material damping because the waves propagated through the site profile (e.g., Campbell, 2009) and can be calculated in a variety of ways depending on the size of the earthquake and the available recordings (Ktenidou *et al.*, 2014). We use κ_0 to define the site attenuation because of its common use in engineering seismology (Campbell, 2009; Ktenidou *et al.*, 2014).

Site Characterization in CENA. Campbell (2003) and Tavakoli and Pezeshk (2005) used a CENA reference hard-rock site condition with a time-average shear-wave velocity in the top 30 m of the site profile of $V_{S30} \approx 2800$ m/s and $\kappa_0 = 0.006$ s. They used the generic CENA hard-rock crustal-amplification model developed by Boore and Joyner (1997). Atkinson and Boore (2006), Pezeshk *et al.* (2011), and Campbell (2008, 2011) used an empirically derived CENA hard-rock crustal-amplification model corresponding to $V_{S30} \ge 2000$ m/s and $\kappa_0 = 0.005$ s (Atkinson and Boore, 2006). In this study, we adopted a CENA reference hard-rock site condition more recently recommended by Hashash, Kottke, Stewart, Campbell, Kim, Moss, *et al.* (2014) for use in the NGA-East project that corresponds to $V_{S30} = 3000$ m/s and $\kappa_0 = 0.006$ s based on the comprehensive studies of Campbell *et al.* (2014) and Hashash, Kottke, Stewart, Campbell, Kim, Rathje, *et al.* (2014). We used the crustal-amplification factors derived by Boore and Thompson (2015) using the SRI method, which are based on the velocity profile of Boore and Joyner (1997) modified to have a shear-wave velocity of 3000 m/s over the top 300 m of the site profile to be consistent with the NGA-East reference hard-rock crustal profile of Hashash, Kottke, Stewart, Campbell, Kim, Moss, *et al.* (2014). These crustal-amplification factors are listed in Table 1.

Site Characterization in WNA. Boore and Joyner (1997) provided crustal-amplification factors for a generic-rock site profile in WNA with $V_{S30} = 620$ m/s that was developed using the SRI method. These amplification factors have been used by many investigators, including the authors, to conduct stochastic simulations in the region (e.g., Atkinson and Silva, 1997, 2000; Beresnev and Atkinson, 2002; Campbell, 2003, 2007, 2008, 2011; Tavakoli and Pezeshk, 2005; Pezeshk *et al.*, 2011, 2015). Boore and Thompson (2014, 2015) updated the generic-rock crustal-amplification factors of Boore and Joyner (1997), using an improved density–velocity relationship, which we adopted for our study. These updated crustal-amplification factors are listed in Table 1.

Anderson and Hough (1984) report typical values for κ_0 in 0.02–0.04 s range for rock sites in WNA. Atkinson and Silva (1997) used an average value of 0.04 s in their stochastic model for southern California, which has been used by many other investigators, including the authors. Yenier and

Table 1
Crustal-Amplification Factors (Boore and Thompson, 2015)

CENA (Table 5 of Boore and Thompson, 2015)		WNA (Table 4 of Boore and Thompson, 2015)	
f (Hz)	$A(f)$	f (Hz)	$A(f)$
0.001	1.000	0.001	1.00
0.008	1.003	0.009	1.01
0.023	1.010	0.025	1.03
0.040	1.017	0.049	1.06
0.061	1.026	0.081	1.10
0.108	1.047	0.150	119
0.234	1.069	0.370	1.39
0.345	1.084	0.680	1.58
0.508	1.101	1.110	1.77
1.090	1.135	2.360	2.24
1.370	1.143	5.250	2.75
1.690	1.148	60.30	4.49
1.970	1.150	100.0	4.49
2.420	1.151		

Crustal-amplification factor do not include the effects of site attenuation. CENA, central and eastern North America; WNA, western North America.

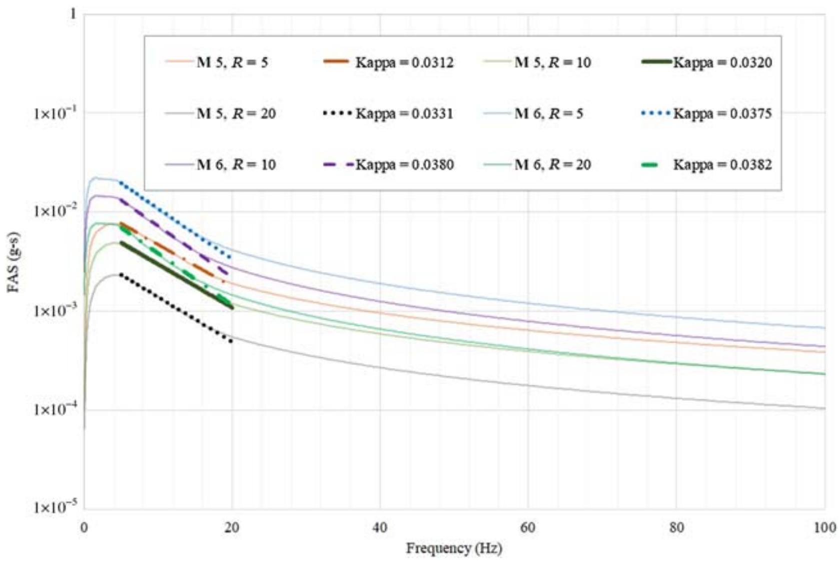

Figure 1. Kappa values in seconds for six scenarios computed from the median of the Next Generation Attenuation-West2 (NGA-West2) ground-motion prediction equations (GMPEs) using the inverse random vibration theory (IRVT) approach. FAS, Fourier amplitude spectrum. The color version of this figure is available only in the electronic edition.

Atkinson (2015b) found that a value of 0.025 s was consistent with ground-motion recordings on rock in California. Following Al Atik *et al.* (2014), we used inverse random vibration theory (IRVT) to derive a value for the host site kappa in WNA that is consistent with the NGA-West2 GMPEs and the generic-rock amplification factors of Boore and Thompson (2014, 2015). The single value of kappa that we are using is consistent with the values found by Zandieh *et al.* (2016) for the magnitudes and distances of interest. We removed the host crustal-amplification factors from the IRVT-based near-source FAS predictions to decouple the crustal-amplification term from the κ_0 term at high frequencies as suggested by Al Atik *et al.* (2014). The resulting FAS were analyzed to select the start and end frequencies over which plots of log FAS versus frequency could be considered linear and not impacted by high-frequency distortions from the predicted response spectra. Then we fit a slope of $-\pi\kappa_0$ to the selected range of frequencies. Similar to Al Atik *et al.* (2014), we considered six different near-source scenarios (**M** 5.0 and 6.0; $R_{\mathrm{rup}} = 5$, 10, and 20 km) to define kappa values for the median of the GMIM predictions from all five NGA-West2 GMPES. We limited the magnitude range to 6.0 to be consistent with the range used in the inversions of the NGA-West2 GMPEs. Figure 1 illustrates how the kappa values were calculated by the IRVT approach for the six scenarios. These results are consistent with an average κ_0 of 0.035 s, which we used to characterize the site attenuation for the generic-rock site in WNA (Table 2).

Source Model

We used the Brune (1970, 1971) ω^2 source spectrum in the stochastic simulations. Brune's model is a single-corner-frequency (f_0) point-source spectrum in which the stress parameter $\Delta\sigma$ controls the spectral shape at high frequencies. The choice of an appropriate stress parameter in WNA and CENA has been the subject of many studies. The basis for the values of $\Delta\sigma$ we use for these regions is discussed in the following sections.

Stress Parameter in CENA. Boore *et al.* (2010) used the point-source stochastic simulation program SMSIM (Boore, 2005) to determine the stress parameters for eight well-recorded earthquakes in CENA. They showed that estimates of $\Delta\sigma$ are strongly correlated to the rate of geometrical spreading in the near-source region. They estimated a geometric mean value of $\Delta\sigma = 250$ bars using the geometrical spreading and quality factor (Q) relationships of Atkinson

Table 2
Median Values of Seismological Parameters for Stochastic Simulations

Parameter	WNA	CENA
Source spectrum model	Single-corner-frequency ω^{-2}	Single-corner-frequency ω^{-2}
Stress parameter, $\Delta\sigma$ (bars)	135	400
Source velocity, β_S (km/s)	3.5	3.7
Source density, ρ_S (g/cc)	2.8	2.8
Geometric spreading, $Z(R)$	$\begin{cases} R^{-1.03} & R < 45\ \text{km} \\ R^{-0.96} & 45 \le R < 125\ \text{km} \\ R^{-0.50} & R \ge 125\ \text{km} \end{cases}$	$\begin{cases} R^{-1.3} & R < 60\ \text{km} \\ R^{0} & 60 \le R < 120\ \text{km} \\ R^{-0.50} & R \ge 120\ \text{km} \end{cases}$
Quality factor, Q	$202f^{0.54}$	$440f^{0.47}$
Source duration, T_S (s)	$1/f_0$	$1/f_0$
Path duration, T_P (s)	Boore and Thompson (2015, their table 1)	Boore and Thompson (2015, their table 2)
Crustal amplification, $A(f)$	Boore and Thompson (2015, their table 4)	Boore and Thompson (2015, their table 5)
Site kappa, κ_0 (s)	0.035	0.006 (Hashash, Kottke, Stewart, Campbell, Kim, Moss, *et al.*, 2014)

(2004; hereafter, A04) for the case in which the 1988 Saguenay earthquake was included and 180 bars for the case in which the Saguenay event was excluded. Atkinson *et al.* (2009) and Boore (2009) also found that a stress parameter of 250 bars instead of 140 bars was needed to bring the stochastic point-source results of SMSIM in line with the stochastic finite-fault results of EXSIM (Motazedian and Atkinson, 2005), which was used to develop the GMPE of Atkinson and Boore (2006), for small distant earthquakes. Campbell (2008, 2011) had initially estimated this point-source stress parameter as $\Delta\sigma = 280$ bars. Atkinson and Assatourians (2010) analyzed recordings of the **M** 5.0 Val-des-Bois, Quebec, earthquake using the A04 attenuation model and found a stress parameter of 250 bars.

In their revision of the CENA seismological model, Boore and Thompson (2015) found that a stress parameter of 400 bars was needed to approximate the amplitude of the ground motions that matched the A04 attenuation term and the Atkinson and Boore (1995) path duration when the new energy-based significant duration parameter recommended by Boore and Thompson (2014) was used. A higher value of $\Delta\sigma$ was needed to compensate for the smaller amplitudes predicted from the stochastic ground-motion simulations when the longer path durations were used, which spreads the radiated energy from the point source over a longer duration. Because we are using the new path duration model of Boore and Thompson (2015), for consistency, we also use $\Delta\sigma = 400$ bars for our CENA point-source stochastic simulations (Table 2).

Stress Parameter in WNA. Atkinson and Silva (1997, 2000) modeled California ground motions using the stochastic finite-fault simulation model of Silva *et al.* (1990). They introduced an equivalent two corner-frequency point-source spectrum to mimic the finite-fault effects observed at large magnitudes in lieu of using a variable stress parameter as used in the GMPEs of Silva *et al.* (2002) and Yenier and Atkinson (2015b). They showed that at high frequencies, their double-corner-frequency source model gave similar results for events of $\mathbf{M} < 6.0$ as a Brune single-corner-frequency model with $\Delta\sigma = 80$ bars. At larger magnitudes and lower frequencies, in which finite-fault effects become significant, the two models were found to diverge because of the spectral sag in the double-corner model that was found to more realistically model the spectral shape of large-magnitude ground motions. Yenier and Atkinson (2015b) proposed a seismological model for California that they empirically calibrate with response spectra from the NGA-West2 database. Crustal-amplification factors were derived using the SRI method and the NEHRP B/C ($V_{S30} = 760$ m/s) velocity profile with an assumed site attenuation parameter of $\kappa_0 = 0.025$ s (Yenier and Atkinson, 2014). The source was defined as a Brune single-corner spectrum. Path attenuation was adopted from Raoof *et al.* (1999) but was modified to represent a different crustal shear-wave velocity and to have a minimum path attenuation of $Q = 100$. Path duration was taken from Boore and Thompson (2014). Geometric spreading was found to be consistent with $R^{-1.3}$ out to 50 km, after which an $R^{-0.5}$ was used. Yenier and Atkinson (2015b) used the effective point-source distance metric of Atkinson and Silva (2000) for $\mathbf{M} < 6.0$ and that of Yenier and Atkinson (2014) for larger magnitudes to model magnitude-saturation effects. They selected stress parameters that minimized the trends in the residuals, ensuring that the observed and simulated spectra had similar shapes for $f > 0.1$ Hz. These stress parameters were found to be a function of magnitude with values that increase from 15 bars at **M** 3.0 to 100 bars at $\mathbf{M} > 5.0$. Finally, they used a calibration factor of 4.47 in the stochastic simulations to eliminate any bias between the simulated and observed spectral amplitudes. For our stochastic simulations in WNA, we performed an inversion of the NGA-West2 GMPEs for earthquake scenarios with $\mathbf{M} \leq 6.0$. This model was used to ensure that the WNA host seismological model was consistent with the GMIM predictions from the GMPEs that are used to derive the CENA target GMIMs. To minimize the inherent trade-off between κ_0 and $\Delta\sigma$ in these inversions, we used the IRVT method of Al Atik *et al.* (2014) to determine the value of κ_0 from the median near-source estimates of PSA from all five NGA-West2 GMPEs, as described earlier in the report. The IRVT approach resulted in an average site kappa of $\kappa_0 = 0.035$ s. After constraining κ_0 to the average obtained from the IRVT approach and constraining the crustal amplifications to those suggested by Boore and Thompson (2015), we performed GMIM inversions to obtain the remaining seismological parameters using a genetic algorithm similar to that of Scherbaum *et al.* (2006). By constraining the crustal-amplification factors and the value of κ_0, the near-source spectral shape at high frequencies becomes a function of only the stress parameter, which helped to stabilize the inversion results.

Based on the inversions, we obtained a stress parameter of 135 bars for scenarios in **M** 4.0–6.0 range. We used this stress parameter for all magnitudes to be consistent with the magnitude-independent stress parameter that was used in the CENA seismological model. Pezeshk *et al.* (2011) used a stress parameter of 80 bars in their WNA Brune single-corner-frequency stochastic model, which they showed was generally consistent with the NGA-West1 GMPE predictions for an **M** 6.0 earthquake at $R_{\mathrm{rup}} = 10$ km. The larger stress parameter of 135 bars found is consistent with the longer path durations associated with the Boore and Thompson (2015) WNA duration model and supersedes the value used by Pezeshk *et al.* (2011). A stress parameter of 135 bars is also consistent with observations of modified Mercalli intensity by Atkinson and Wald (2007), who suggested that these observations were consistent with about a three-times-larger stress parameter for earthquakes in CENA compared with those in WNA, consistent with the values used in this study (Table 2).

Source and Path Duration

The sum of the source duration (T_S) and the path duration (T_P) represents the total duration of ground motion in the stochastic method. The source duration for the Brune single-corner-frequency model is typically defined (e.g., Boore, 2003) as the inverse of the source corner frequency, $1/f_0$ (Table 2). Boore and Thompson (2014) used the NGA-West2 database to derive a new distance-dependent T_P relationship for active crustal regions, such as WNA, which is different from the relationships proposed previously. Similarly, Boore and Thompson (2015), using the NGA-East database (Goulet *et al.*, 2014; see Data and Resources), derived a distance-dependent T_P relationship for CENA. We used the path-duration terms proposed by Boore and Thompson (2014, 2015) in this study, which are provided in Table 3 for completeness.

Path Attenuation

The path term $P(R, f)$ in equation (1) is separated into two components, commonly referred to as geometric attenuation (or spreading) and anelastic attenuation. Geometric attenuation models the amplitude decay due to the expanding surface area of the wave front as it propagates away from the source. Anelastic attenuation, quantified by the quality factor Q, models the amplitude decay caused by scattering and the conversion of elastic wave energy to heat and is usually found to be frequency dependent. The path-attenuation parameters that we used for CENA and WNA are presented in the following sections.

Path Attenuation for CENA. Boore *et al.* (2010) used four geometrical attenuation models ranging from a simple $R^{-1.0}$ decay for all distances to more complicated bilinear and trilinear distance decay models to determine the stress parameter for eight well-recorded earthquakes in CENA. Atkinson and Assatourians (2010) studied five well-recorded CENA earthquakes and found that the ground motions were better fit if the A04 geometrical attenuation model, with $R^{-1.3}$ near-source spreading, is used for hypocentral distances beyond 10 km and an $R^{-1.0}$ decay is used at shorter distances. Campbell (2007, 2008, 2011) and Pezeshk *et al.* (2011) used the original A04 path-attenuation model.

In this study, we used the more recent path-attenuation term developed by Chapman *et al.* (2014) in our CENA seismological model (Table 2). These authors used broadband recordings from the EarthScope Transportable Array and an iterative inversion process to derive a trilinear geometric attenuation model with $R^{-1.3}$ spreading to 60 km, R^0 or no spreading from 60 to 120 km, and $R^{-0.5}$ or *Lg* spreading beyond 120 km. At regional distances, the dominant phase in the ground-motion recording is the *Lg* phase, which is composed of multiple reflections of *S* waves trapped within the crust. Chapman and Godbee (2012) also found $R^{-1.3}$ spreading at short distances from physics-based ground-motion simulations. Chapman *et al.* (2014) found that for all CENA regions outside of the Gulf Coast region, the quality factor that is consistent with the above geometric attenuation term is given by the relationship $Q = 440f^{0.47}$. As illustrated in Figure 2, the transition distances of 60 and 120 km in the Chapman *et al.* (2014) geometric attenuation model are nearly the same and therefore consistent with the transition distances obtained by Boore and Thompson (2015) for their CENA path-duration model. Furthermore, to show that our parameters are consistent, we compared the FAS based on our model with a model using A04 seismological parameters and stress drop of 400 for moment magnitudes of 4, 5, 6, and 7 and found almost identical results.

Path Attenuation for WNA. Campbell (2007, 2008, 2011) and Pezeshk *et al.* (2011, 2015) used the path-attenuation model of Raoof *et al.* (1999) developed for southern California in their stochastic point-source ground-motion simulations in WNA. Atkinson and Silva (2000) also used this path-attenuation model in their stochastic finite-fault simulations. Malagnini *et al.* (2007) analyzed broadband waveforms from small to moderate events in the San Francisco Bay area and found that the best-fitting path-attenuation model was given by the relationship $Q = 180f^{0.42}$ for geometric attenuation given by $R^{-1.0}$ spreading within 30 km and $R^{-0.6}$ spreading at larger distances. This model is similar to that of Raoof *et al.* (1999), who found $Q = 180f^{0.45}$ for geometric attenuation given by $R^{-1.0}$ spreading within 40 km and $R^{-0.5}$ spreading at larger distances. Fatehi and Herrmann (2008) determined high-frequency scaling in the Pacific Northwest and northern and central California by analyzing broadband waveforms in these regions. They found both geometric and anelastic attenuation to be regionally dependent. Spreading rates were found to vary between $R^{-1.0}$ and $R^{-1.1}$ within 40 km, except for very high frequencies in northern California, which had a rate of $R^{-1.3}$. Spreading rates at longer distances were found to be more variable, ranging from $R^{-0.8}$ to $R^{0.5}$ from distances of 40 to 100 km and $R^{-0.5}$ to $R^{-0.9}$ at larger distances. Anelastic attenuation

Table 3
Path-Duration Models (Boore and Thompson, 2015)

CENA (Table 2 of Boore and Thompson, 2015)		WNA (Table 1 of Boore and Thompson, 2015)	
R_{rup} (km)*	T_P (s)	R_{rup} (km)	T_P (s)
0	0.0	0.0	0.0
15	2.6	7.0	2.4
35	17.5	45.0	8.4
50	25.1	125.0	10.9
125	25.1	175.0	17.4
200	28.5	270.0	34.2
392	46.0		
600	69.1		
Slope of last segment	0.111	Slope of last segment	0.156

*Rupture distance must be converted to the effective point-source distance using the pseudodepth appropriate for each magnitude.

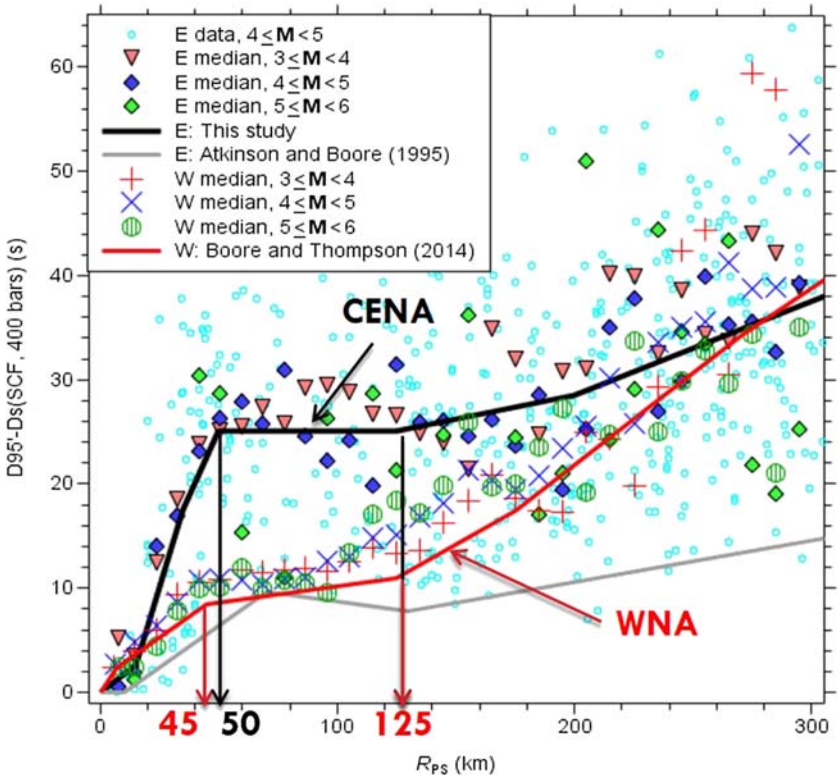

Figure 2. Path-duration models for central and eastern North America (CENA) and western North America (WNA; modified from Boore and Thompson, 2015). In the legend, E represents eastern North America, and W represents western North America. The color version of this figure is available only in the electronic edition.

parameters were also found to be variable with $Q_0 = 210$–280 and $\eta = 0.35$–0.55, depending on the region.

Mahani and Atkinson (2013) investigated the rate of geometric attenuation of ground motion from small-to-moderate earthquakes across North America and found spreading rates that varied between $R^{-1.1}$ and $R^{-1.3}$ at near-source distances. At longer distances, typically beyond 40–100 km, ground motions are dominated by surface waves for which the path attenuation depends on fault mechanism, focal depth, and crustal structure (Burger *et al.*, 1987; Ou and Herrmann, 1990; Yenier and Atkinson, 2015b). Yenier and Atkinson (2014) found that geometric spreading from 11 well-recorded earthquakes in California is generally steeper than $R^{-1.0}$ at short distances. Yenier and Atkinson (2015b) considered a bilinear geometric spreading term and near-source spreading rates of both $R^{-1.0}$ and $R^{-1.3}$, decreasing to $R^{-0.5}$ beyond a transition distance of 50 km. They determined that both of these near-source spreading rates could be made to fit the recordings using average calibration factors of 1.08 and 3.16, respectively, to adjust the stochastic point-source simulation GMIMs over all magnitudes and frequencies. They concluded that the steeper near-source spreading rate provided the best fit to the path attenuation in California. As discussed previously, Yenier and Atkinson (2015b) used the Raoof *et al.* (1999) anelastic attenuation term, which after scaling to a shear-wave velocity of 3.7 km/s in the vicinity of the source, was modified to $Q = \max(100, 170.3 f^{0.45})$. The maximum value of 100 was based on the recommendations of Boore (1983) and Yenier and Atkinson (2014).

In this study, we used the path-attenuation terms determined from the inversion of the NGA-West2 GMPEs. For consistency with the CENA seismological model, a trilinear geometric attenuation term with transition distances of 45 and 125 km was used to perform the inversions. These transition distances were selected to match the WNA transition distances used by Boore and Thompson (2015) in their path-duration model (Fig. 2). The inversion resulted in a geometric spreading rate of $R^{-1.0}$ to 125 km (i.e., no difference for $R < 45$ km), beyond which an assumed spreading rate of $R^{-0.5}$ consistent with surface-wave attenuation was used (Table 3). The resulting anelastic attenuation term was found to be $Q = 202 f^{0.54}$ (Table 2), similar to that found by Campbell (2007) using ground-motion predictions from the Campbell and Bozorgnia (2008) NGA-West1 GMPE and by Atkinson and Silva (1997) using ground motions from the WNA strong-motion database.

GMPEs for WNA

One important component of the HEM approach is using appropriate empirical GMPEs in the host region. Pezeshk *et al.* (2011) incorporated the five GMPEs from the PEER NGA-West1 project (Power *et al.*, 2008) to derive empirical ground-motion estimates for WNA in their HEM-based GMPE for CENA. Campbell (2007, 2008, 2011) used a single NGA-West1 GMPE (Campbell and Bozorgnia, 2008) to demonstrate how the new NGA-West1 models might impact the Campbell (2003) HEM-based GMPE in CENA.

In this study, we used the five GMPEs developed as part of the PEER NGA-West2 project (Bozorgnia *et al.*, 2014) to derive the empirical GMIM estimates in the WNA host region. These GMPEs are referred to as ASK14 (Abrahamson *et al.*, 2014), BSSA14 (Boore *et al.*, 2014), CB14 (Campbell and Bozorgnia, 2014), CY14 (Chiou and Youngs, 2014), and I14 (Idriss, 2014) in the remainder of this article. These GMPEs used a vastly expanded NGA-West2 database that included more than 20,000 recordings from shallow crustal earthquakes in California (**M** < 5.5) and in other similar active tectonic regions throughout the world (**M** > 5.5). We used the weighted geometric mean of the RotD50 (Boore, 2010) average horizontal GMIM predictions from the five GMPEs to derive empirical estimates that are consistent with the inversions performed. We assigned the same weights that were used to evaluate the NGA-West2 GMPEs for the 2014 update of the United States national seismic hazard model (Petersen *et al.*, 2014). In this scheme, the weights were distributed evenly between four of the GMPEs with I14 being given half the weight of the other models.

Except for the BSSA14 model, which is developed for the R_{JB} distance metric, the other GMPEs use the closest distance to the fault-rupture surface, represented by the R_{rup} distance metric. Because the proposed model in this study is based on R_{rup}, we converted R_{JB} to R_{rup} for evaluating the BSSA14 model using the relationships developed by Scherbaum *et al.* (2004). Following Campbell (2003, 2007), we used a generic style of faulting to evaluate the NGA-West2 GMPEs, because there is no empirical evidence in CENA that there are differences in ground-motion amplitude between faulting styles. This generic style of faulting is an average of strike-slip and reverse-faulting mechanisms because of the predominantly compressional stress regime in CENA, and was implemented by setting $F_{\mathrm{RV}} = 0.5$ and $F_{\mathrm{NM}} = 0$ in the ASK14, CB14, and CY14 GMPEs; SS = 0.5 (strike slip), RS = 0.5 (reverse slip), NS = 0 (normal slip), and $U = 0$ (unknown slip) in the BSSA14 GMPE, and the source mechanism $F = 0.5$ in the I14 GMPE. We did not include the hanging-wall effect in the evaluation of the ASK14, CB14, and CY14 models because of the unknown strikes of earthquakes and the general absence of known faults in CENA. All the NGA-West2 GMPEs that included regional site-response and anelastic attenuation terms were evaluated for the California region and for NEHRP B/C (Building Seismic Safety Council [BSSC], 2009) site conditions consistent with $V_{S30} = 760$ m/s. The CY14 GMPE was evaluated for average directivity effects and for an inferred value of V_{S30}, which only affects the value of the standard deviation. We used a dip of 90° to evaluate those GMPEs that had the dip of the fault-rupture plane as a predictor variable.

The ASK14, CB14, and CY14 GMPEs include the depth to the top of rupture Z_{TOR} as one of the predictor variables. For each of these models, the default value of Z_{TOR} recommended by the developers for a future California earthquake was used. The ASK14, BSSA14, and CY14 GMPEs use $Z_{1.0}$, or the depth to the 1 km/s shear-wave velocity (V_S) horizon beneath the site, to model sediment-depth and basin effects. The CB14 GMPE uses $Z_{2.5}$, or the depth to the $V_S = 2.5$ km/s horizon beneath the site, to model these effects. For these GMPEs, the default values of $Z_{1.0}$ and $Z_{2.5}$ recommended by each of the developers for a California site were used.

GMPEs for CENA

Median estimates of the desired GMIMs in CENA are obtained by scaling the NGA-West2 empirical estimates of PGA and PSA with the stochastically derived adjustment factors derived using a set of computer routines based on the random vibration method of Kottke and Rathje (2008) with the sets of seismological parameters listed in Table 2. The GMIMs are evaluated for 9 values of magnitude ranging from **M** 4.0 to 8.0 in 0.5 magnitude increments and for 25 values of distance given by the array $R_{\mathrm{rup}} = 1$, 2, 5, 10, 15, 20, 30, 40, 50, 60, 70, 80, 100, 120, 140, 180, 200, 250, 300, 400, 500, 600, 700, 800, and 1000 km. Because the GMPEs were developed for a CENA reference hard-rock site with $V_{S30} = 3000$ m/s and $\kappa_0 = 0.006$ s (Hashash, Kottke, Stewart, Campbell, Kim, Moss, *et al.*, 2014), the GMIM predictions must be modified for other site conditions using an appropriate site-response method.

A limitation of the empirical GMIM estimates and, therefore, the HEM approach is the general invalidity of the NGA-West2 GMPEs beyond distances of around 300 km. Because of the lower rate of attenuation in CENA, GMIM amplitudes of engineering significance can occur at distances farther than 300 km and possibly as far as 1000 km for the **M** 7.5–8.0 events as occurred in New Madrid in 1811 and 1812 (Petersen *et al.*, 2014). To handle this limitation in the pre-NGA GMPEs, Campbell (2003) supplemented the GMIMs that were estimated from the HEM approach for CENA with stochastically simulated GMIMs for $R_{\mathrm{rup}} > 70$ km. He scaled the stochastically simulated GMIMs for each magnitude by a factor that made them equal to the median HEM estimate for the same magnitude at $R_{\mathrm{rup}} = 70$ km. Tavakoli and Pezeshk (2005) and Pezeshk *et al.* (2011) used the same approach in the development of their HEM-based models. Campbell (2008, 2011) also used the same approach to scale the empirical GMIM estimates from the Campbell and Bozorgnia (2008) NGA-West1 GMPE, which although was nominally valid to distances of 200 km, was practically only valid to around 100 km. Although the approach used previously is perfectly valid, we decided to use a different procedure in this study. We used the HEM approach to estimate GMIMs to the maximum distance of 1000 km and then compared these estimates with recordings from the NGA-East CENA database (Goulet *et al.*, 2014; see Data and Resources). We used a calibration factor to adjust any bias that existed between the GMIM estimates from the HEM approach and the CENA observations. A single calibration factor was used for all magnitudes, distances, and spectral periods to prevent any distortions in the shape of the predicted response spectra.

After calibration, the HEM-simulated GMIMs were used together with nonlinear least-squares regression to derive the model coefficients in a GMPE defined with a specified functional form. GMPEs were developed for PGA and for 5% damped PSA for $\mathbf{M} \le 6$, $R_{\mathrm{rup}} \le 1000$ km and 21 spectral periods ranging from $T = 0.01$ to 10 s, consistent with the set of periods used in the NGA-West2 models. Magnitude scaling for $\mathbf{M} > 6$ was estimated using two methods, referred to as stochastic scaling and empirical scaling. These methods are described later in this section. After trial and error, the GMPE functional form that was found to best model the HEM GMIM estimates is given by the expression:

$$\log(\bar{Y}) = c_1 + c_2\mathbf{M} + c_3\mathbf{M}^2 + (c_4 + c_5\mathbf{M}) \times \min[\log(R), \log(60)] + (c_6 + c_7\mathbf{M}) \times \max[\min\{\log(R/60), \log(120/60)\}, 0] + (c_8 + c_9\mathbf{M}) \times \max[\log(R/120), 0] + c_{10}R, \quad (4)$$

in which

$$R = \sqrt{R_{\mathrm{rup}}^2 + C_{11}^2}. \quad (5)$$

In equations (4) and (5), $\bar{Y}$ is the median value of PGA or PSA (g), $\mathbf{M}$ is moment magnitude, and R_{rup} is the closest distance to the fault-rupture surface (km). The coefficients in these equations are given in Tables 4 and 5 for the large-magnitude stochastic-scaling and empirical-scaling methods, respectively.

The aleatory variability characterizes the inherent randomness in the predicted GMIMs that result from any unmodeled characteristics of the ground motion (Campbell, 2007). In this study, we constructed the mean aleatory variability model from the weighted average of the standard deviations of the five NGA-West2 GMPEs, similar to the approach of Campbell (2003, 2007), Tavakoli and Pezeshk (2005), and Pezeshk *et al.* (2011, 2015). Except for I14, the other four NGA-West2 GMPEs partition the total standard deviation σ into components that represent between-event variability (τ) and within-event variability (ϕ). We used the weighted average of the between-event and within-event standard deviations from these four NGA-West2 models to derive the aleatory variability model proposed in this study. All of the NGA-West2 GMPEs have standard deviations that vary with magnitude and some that vary with distance and site conditions. Because the GMPEs were evaluated for firm-rock site conditions, the dependence on site conditions could be neglected. Also, because of the relatively weak distance dependence of the average standard deviations, we chose to simplify the model by excluding distance as a parameter and instead averaged the standard deviations over the 25 distance values used to evaluate the NGA-West2 GMPEs for each magnitude. The resulting natural log standard deviations are given by the following expressions:

$$\tau = \begin{cases} c_{12} & \mathbf{M} \le 4.5 \\ c_{13} + c_{14}\mathbf{M} & 4.5 < \mathbf{M} \le 5.0 \\ c_{15} + c_{16}\mathbf{M} & 5.0 < \mathbf{M} \le 6.5 \\ c_{17} + c_{18}\mathbf{M} & \mathbf{M} > 6.5 \end{cases} \quad (6)$$

and

$$\phi = \begin{cases} c_{19} + c_{20}\mathbf{M} & \mathbf{M} \le 4.5 \\ c_{21} + c_{22}\mathbf{M} & 4.5 < \mathbf{M} \le 5.0 \\ c_{23} + c_{24}\mathbf{M} & 5.0 < \mathbf{M} \le 6.5 \\ c_{25} & \mathbf{M} > 6.5 \end{cases}. \quad (7)$$

The total aleatory standard deviation, excluding the variability of the regression, is calculated from the between-event and within-event standard deviations by the equation:

$$\sigma_{\log \bar{Y}} = \sqrt{\tau^2 + \phi^2}. \quad (8)$$

The total aleatory standard deviation that includes the variability of the regression is given by the equation:

$$\sigma_T = \sqrt{\sigma_{\log \bar{Y}}^2 + \sigma_{\mathrm{Reg}}^2}, \quad (9)$$

in which σ_{Reg} is the standard deviation of the regression. The model misfit is much smaller than the other aleatory variability components and can be neglected for many seismic hazard applications (e.g., Pezeshk *et al.*, 2011). σ_{Reg} coefficients are listed in Tables 4 and 5, respectively. The coefficients in equations (6) and (7) are listed in Tables 6 and 7, respectively. Even though the GMPE is given in terms of common logarithms, the standard deviations are given in terms of natural logarithms. This is done to be consistent with the natural log standard deviations of the NGA-West2 GMPEs and the common means of reporting these standard deviations in the literature.

It should be noted that an evaluation of epistemic uncertainty is not included in this study. Based on the mathematical framework given in Campbell (2003), the major sources of epistemic uncertainty in the HEM approach are due to (1) uncertainty in the seismological parameters used in the stochastic simulations and (2) uncertainty in the empirical GMPEs. We did not include epistemic uncertainty in our model because, in practice, this type of uncertainty is typically evaluated using alternative GMPEs and the within-model uncertainty associated with an individual GMPE, such as that proposed by Al Atik and Youngs (2014), is not generally included (e.g., Campbell, 2007, 2014; Pezeshk *et al.* 2011).

The GMIM predictions from the empirical GMPEs used in the inversions performed to develop the WNA stochastic model seismological parameters were limited to events with $\mathbf{M} \le 6.0$ to limit them to a range of magnitudes for which the point-source assumption used in the stochastic simulations is valid. Therefore, we believe that HEM-based GMIM estimates and the WNA and CENA stochastic models used to derive them are well constrained by empirical data for $\mathbf{M} \le 6.0$, after applying an average empirical calibration factor of 0.32 (a factor of 2.09) to the HEM estimates. This calibration factor is included in the c_1 coefficient of equation (4). For events with $\mathbf{M} > 6$, we considered two approaches to account for magnitude scaling (1) using the HEM-based simulations for all magnitudes, assuming that the HEM approach can be extrapolated to magnitudes larger than those used to develop the WNA and CENA seismological models (hereafter referred to as the stochastic-scaling approach) using the assumed $h(\mathbf{M})$ and (2) using the HEM simulations to model magnitude scaling for $\mathbf{M} \le 6.0$ and using the magnitude scaling predicted by the NGA-West2

Table 4
Coefficients and Standard Deviations of Regression for the Stochastic-Scaling Approach

T (s)	c_1	c_2	c_3	c_4	c_5	c_6	c_7	c_8	c_9	c_{10}	c_{11}	σ_{Reg}
PGA	-2.043×10^{-1}	7.805×10^{-1}	-8.063×10^{-2}	−3.956	3.901×10^{-1}	-3.259×10^{-1}	8.243×10^{-2}	−1.928	2.511×10^{-1}	-2.347×10^{-3}	−6.368	6.757×10^{-2}
0.01	4.265×10^{-1}	7.075×10^{-1}	-7.832×10^{-2}	−4.184	4.091×10^{-1}	-6.455×10^{-1}	1.049×10^{-1}	−2.056	2.585×10^{-1}	-2.286×10^{-3}	6.653	6.683×10^{-2}
0.02	6.573×10^{-1}	6.803×10^{-1}	-7.444×10^{-2}	−4.088	3.909×10^{-1}	-6.327×10^{-1}	5.930×10^{-2}	−2.645	2.934×10^{-1}	-2.045×10^{-3}	6.723	7.019×10^{-2}
0.03	3.420×10^{-1}	7.205×10^{-1}	-7.437×10^{-2}	−3.896	3.729×10^{-1}	6.628×10^{-3}	-1.971×10^{-2}	−2.848	3.026×10^{-1}	-2.068×10^{-3}	6.523	7.611×10^{-2}
0.04	-1.266×10^{-2}	7.652×10^{-1}	-7.558×10^{-2}	−3.753	3.644×10^{-1}	5.479×10^{-1}	-6.757×10^{-2}	−2.577	2.711×10^{-1}	-2.376×10^{-3}	−6.332	8.139×10^{-2}
0.05	-2.608×10^{-1}	7.963×10^{-1}	-7.698×10^{-2}	−3.683	3.639×10^{-1}	7.904×10^{-1}	-7.123×10^{-2}	−2.094	2.232×10^{-1}	-2.747×10^{-3}	−6.190	8.635×10^{-2}
0.08	-7.995×10^{-1}	9.087×10^{-1}	-8.460×10^{-2}	−3.587	3.591×10^{-1}	6.022×10^{-1}	3.520×10^{-3}	−1.075	1.398×10^{-1}	-3.319×10^{-3}	6.105	9.263×10^{-2}
0.10	−1.391	1.060	-9.486×10^{-2}	−3.475	3.439×10^{-1}	2.369×10^{-1}	6.864×10^{-2}	-4.517×10^{-1}	8.967×10^{-2}	-3.481×10^{-3}	6.130	9.041×10^{-2}
0.15	−2.425	1.322	-1.117×10^{-1}	−3.322	3.177×10^{-1}	-3.225×10^{-1}	1.450×10^{-1}	1.825×10^{-1}	8.081×10^{-3}	-3.216×10^{-3}	6.229	8.438×10^{-2}
0.20	−3.243	1.537	-1.262×10^{-1}	−3.278	3.062×10^{-1}	-5.643×10^{-1}	1.689×10^{-1}	1.641×10^{-1}	-4.100×10^{-3}	-2.638×10^{-3}	6.366	8.335×10^{-2}
0.25	−3.858	1.685	-1.361×10^{-1}	−3.265	3.024×10^{-1}	-6.514×10^{-1}	1.742×10^{-1}	5.760×10^{-2}	-3.273×10^{-3}	-2.137×10^{-3}	6.331	8.384×10^{-2}
0.30	−4.240	1.772	-1.419×10^{-1}	−3.291	3.053×10^{-1}	-6.865×10^{-1}	1.736×10^{-1}	-6.002×10^{-2}	2.221×10^{-3}	-1.744×10^{-3}	6.318	8.163×10^{-2}
0.40	−5.013	1.932	-1.501×10^{-1}	−3.235	2.919×10^{-1}	-6.095×10^{-1}	1.481×10^{-1}	-3.715×10^{-1}	2.499×10^{-2}	-1.072×10^{-3}	6.493	7.561×10^{-2}
0.50	−5.441	2.005	-1.532×10^{-1}	−3.232	2.888×10^{-1}	-5.287×10^{-1}	1.262×10^{-1}	-6.771×10^{-1}	5.550×10^{-2}	-6.642×10^{-4}	6.558	6.897×10^{-2}
0.75	−6.085	2.070	-1.533×10^{-1}	−3.201	2.863×10^{-1}	-4.266×10^{-1}	1.014×10^{-1}	-9.856×10^{-1}	8.410×10^{-2}	-3.040×10^{-4}	6.303	6.329×10^{-2}
1.00	−6.446	2.077	-1.498×10^{-1}	−3.165	2.814×10^{-1}	-3.605×10^{-1}	8.293×10^{-2}	−1.113	9.241×10^{-2}	-1.857×10^{-4}	6.187	6.259×10^{-2}
1.50	−6.727	1.992	-1.381×10^{-1}	−3.132	2.848×10^{-1}	-2.712×10^{-1}	6.172×10^{-2}	−1.272	1.104×10^{-1}	-4.798×10^{-5}	5.818	6.435×10^{-2}
2.00	−6.801	1.907	-1.289×10^{-1}	−3.162	2.935×10^{-1}	-2.309×10^{-1}	4.892×10^{-2}	−1.438	1.316×10^{-1}	-3.612×10^{-6}	5.655	6.504×10^{-2}
3.00	−6.740	1.729	-1.104×10^{-1}	−3.199	3.019×10^{-1}	-1.443×10^{-1}	2.933×10^{-2}	−1.619	1.535×10^{-1}	1.309×10^{-5}	−5.447	6.739×10^{-2}
4.00	−6.638	1.589	-9.647×10^{-2}	−3.220	3.074×10^{-1}	-1.276×10^{-1}	2.714×10^{-2}	−1.575	1.411×10^{-1}	-4.202×10^{-5}	−5.592	6.594×10^{-2}
5.00	−6.726	1.536	-8.978×10^{-2}	−3.231	3.089×10^{-1}	-1.063×10^{-1}	2.324×10^{-2}	−1.572	1.354×10^{-1}	-9.189×10^{-5}	5.726	6.501×10^{-2}
7.50	−7.194	1.514	-8.441×10^{-2}	−3.236	3.170×10^{-1}	-1.766×10^{-2}	1.731×10^{-2}	−1.658	1.494×10^{-1}	-1.369×10^{-4}	5.846	6.265×10^{-2}
10.00	−7.507	1.522	-8.393×10^{-2}	−3.290	3.257×10^{-1}	1.807×10^{-1}	-3.022×10^{-3}	−1.615	1.461×10^{-1}	-1.939×10^{-4}	5.701	6.838×10^{-2}

Coefficients c_1 to c_{11} are to be used with equations (4) and (9). PGA, peak ground acceleration.

Table 5

Coefficients and Standard Deviations of Regression for the Empirical-Scaling Approach

T (s)	c_1	c_2	c_3	c_4	c_5	c_6	c_7	c_8	c_9	c_{10}	c_{11}	σ_{Reg}
PGA	-7.655×10^{-1}	8.994×10^{-1}	-7.874×10^{-2}	−3.534	2.948×10^{-1}	-4.799×10^{-1}	1.178×10^{-1}	−2.182	3.029×10^{-1}	-2.327×10^{-3}	6.461	5.836×10^{-2}
0.01	-1.871×10^{-1}	8.314×10^{-1}	-7.503×10^{-2}	−3.714	3.030×10^{-1}	-7.793×10^{-1}	1.360×10^{-1}	−2.307	3.093×10^{-1}	-2.263×10^{-3}	6.745	5.637×10^{-2}
0.02	8.387×10^{-2}	7.934×10^{-1}	-7.073×10^{-2}	−3.641	2.898×10^{-1}	-7.692×10^{-1}	9.124×10^{-2}	−2.885	3.399×10^{-1}	-2.013×10^{-3}	6.814	5.774×10^{-2}
0.03	-1.786×10^{-1}	8.256×10^{-1}	-7.148×10^{-2}	−3.489	2.809×10^{-1}	-1.806×10^{-1}	2.319×10^{-2}	−3.072	3.469×10^{-1}	-2.043×10^{-3}	6.616	6.483×10^{-2}
0.04	-4.947×10^{-1}	8.659×10^{-1}	-7.358×10^{-2}	−3.378	2.796×10^{-1}	3.218×10^{-1}	-1.611×10^{-2}	−2.791	3.157×10^{-1}	-2.365×10^{-3}	6.425	7.330×10^{-2}
0.05	-7.246×10^{-1}	8.959×10^{-1}	-7.568×10^{-2}	−3.325	2.831×10^{-1}	5.318×10^{-1}	-1.344×10^{-2}	−2.301	2.693×10^{-1}	-2.751×10^{-3}	6.278	8.156×10^{-2}
0.08	−1.255	1.009	-8.397×10^{-2}	−3.237	2.809×10^{-1}	3.432×10^{-1}	6.065×10^{-2}	−1.289	1.932×10^{-1}	-3.352×10^{-3}	6.184	9.085×10^{-2}
0.10	−1.849	1.160	-9.436×10^{-2}	−3.125	2.660×10^{-1}	1.611×10^{-2}	1.168×10^{-1}	-6.970×10^{-1}	1.511×10^{-1}	-3.519×10^{-3}	−6.205	8.908×10^{-2}
0.15	−2.862	1.418	-1.110×10^{-1}	−2.985	2.416×10^{-1}	-4.494×10^{-1}	1.736×10^{-1}	-1.474×10^{-1}	8.225×10^{-2}	-3.224×10^{-3}	−6.322	8.524×10^{-2}
0.20	−3.666	1.632	-1.256×10^{-1}	−2.952	2.313×10^{-1}	-6.274×10^{-1}	1.847×10^{-1}	-2.470×10^{-1}	7.741×10^{-2}	-2.591×10^{-3}	6.479	8.309×10^{-2}
0.25	−4.260	1.777	-1.355×10^{-1}	−2.955	2.298×10^{-1}	-6.681×10^{-1}	1.811×10^{-1}	-4.060×10^{-1}	8.046×10^{-2}	-2.041×10^{-3}	6.470	8.142×10^{-2}
0.30	−4.630	1.864	-1.416×10^{-1}	−2.995	2.347×10^{-1}	-6.775×10^{-1}	1.760×10^{-1}	-5.479×10^{-1}	8.473×10^{-2}	-1.614×10^{-3}	6.475	7.692×10^{-2}
0.40	−5.407	2.029	-1.506×10^{-1}	−2.950	2.231×10^{-1}	-5.911×10^{-1}	1.492×10^{-1}	-8.400×10^{-1}	9.921×10^{-2}	-9.231×10^{-4}	6.667	6.876×10^{-2}
0.50	−5.843	2.108	-1.545×10^{-1}	−2.956	2.222×10^{-1}	-5.227×10^{-1}	1.298×10^{-1}	−1.086	1.194×10^{-1}	-5.303×10^{-4}	6.733	6.338×10^{-2}
0.75	−6.499	2.185	-1.570×10^{-1}	−2.948	2.259×10^{-1}	-4.594×10^{-1}	1.120×10^{-1}	−1.252	1.284×10^{-1}	-2.316×10^{-4}	6.466	6.348×10^{-2}
1.00	−6.869	2.204	-1.557×10^{-1}	−2.933	2.261×10^{-1}	-4.044×10^{-1}	9.553×10^{-2}	−1.297	1.260×10^{-1}	-1.516×10^{-4}	6.356	6.575×10^{-2}
1.50	−7.172	2.143	-1.484×10^{-1}	−2.940	2.387×10^{-1}	-3.053×10^{-1}	7.187×10^{-2}	−1.386	1.337×10^{-1}	-4.130×10^{-5}	5.986	6.896×10^{-2}
2.00	−7.287	2.085	-1.431×10^{-1}	−2.994	2.533×10^{-1}	-2.546×10^{-1}	5.605×10^{-2}	−1.519	1.494×10^{-1}	-5.530×10^{-6}	−5.806	6.909×10^{-2}
3.00	−7.345	1.957	-1.300×10^{-1}	−3.039	2.649×10^{-1}	-1.506×10^{-1}	3.184×10^{-2}	−1.668	1.648×10^{-1}	7.650×10^{-6}	−5.528	7.060×10^{-2}
4.00	−7.387	1.860	-1.191×10^{-1}	−3.023	2.637×10^{-1}	-1.514×10^{-1}	3.288×10^{-2}	−1.603	1.473×10^{-1}	-4.230×10^{-5}	−5.596	7.011×10^{-2}
5.00	−7.607	1.839	-1.135×10^{-1}	−2.980	2.545×10^{-1}	-1.600×10^{-1}	3.506×10^{-2}	−1.583	1.374×10^{-1}	-9.030×10^{-5}	−5.663	7.060×10^{-2}
7.50	−8.251	1.851	-1.072×10^{-1}	−2.879	2.403×10^{-1}	-1.687×10^{-1}	5.017×10^{-2}	−1.643	1.455×10^{-1}	-1.330×10^{-4}	−5.721	6.987×10^{-2}
10.00	−8.581	1.850	-1.039×10^{-1}	−2.876	2.362×10^{-1}	-8.466×10^{-2}	5.500×10^{-2}	−1.599	1.450×10^{-1}	-2.047×10^{-4}	5.604	7.538×10^{-2}

Coefficients c_1 to c_{11} are to be used with equations (4) and (9).

Table 6
Coefficients of the Between-Event Variability Model in Natural Log Units

Period	C_{12}	C_{13}	C_{14}	C_{15}	C_{16}	C_{17}	C_{18}
PGA	4.191×10^{-1}	7.699×10^{-1}	-7.798×10^{-2}	5.518×10^{-1}	-3.435×10^{-2}	3.596×10^{-1}	-4.792×10^{-3}
0.01	4.188×10^{-1}	7.505×10^{-1}	-7.373×10^{-2}	5.599×10^{-1}	-3.560×10^{-2}	3.596×10^{-1}	-4.792×10^{-3}
0.02	4.245×10^{-1}	8.034×10^{-1}	-8.422×10^{-2}	5.569×10^{-1}	-3.493×10^{-2}	3.610×10^{-1}	-4.790×10^{-3}
0.03	4.416×10^{-1}	8.784×10^{-1}	-9.709×10^{-2}	5.701×10^{-1}	-3.543×10^{-2}	3.716×10^{-1}	-4.885×10^{-3}
0.04	4.571×10^{-1}	9.426×10^{-1}	-1.079×10^{-1}	5.736×10^{-1}	-3.412×10^{-2}	3.853×10^{-1}	-5.163×10^{-3}
0.05	4.725×10^{-1}	1.007	-1.187×10^{-1}	5.772×10^{-1}	-3.286×10^{-2}	3.990×10^{-1}	-5.444×10^{-3}
0.08	4.653×10^{-1}	7.718×10^{-1}	-6.819×10^{-2}	5.843×10^{-1}	-3.068×10^{-2}	4.219×10^{-1}	-5.694×10^{-3}
0.10	4.369×10^{-1}	4.594×10^{-1}	-5.078×10^{-3}	5.920×10^{-1}	-3.159×10^{-2}	4.231×10^{-1}	-5.605×10^{-3}
0.15	4.080×10^{-1}	3.551×10^{-1}	1.173×10^{-2}	5.802×10^{-1}	-3.329×10^{-2}	3.962×10^{-1}	-4.991×10^{-3}
0.20	3.959×10^{-1}	4.398×10^{-1}	-9.744×10^{-3}	5.797×10^{-1}	-3.773×10^{-2}	3.650×10^{-1}	-4.710×10^{-3}
0.25	3.984×10^{-1}	5.748×10^{-1}	-3.920×10^{-2}	5.773×10^{-1}	-3.970×10^{-2}	3.497×10^{-1}	-4.690×10^{-3}
0.30	4.023×10^{-1}	6.887×10^{-1}	-6.367×10^{-2}	5.822×10^{-1}	-4.236×10^{-2}	3.372×10^{-1}	-4.674×10^{-3}
0.40	4.116×10^{-1}	9.150×10^{-1}	-1.119×10^{-1}	5.601×10^{-1}	-4.089×10^{-2}	3.246×10^{-1}	-4.652×10^{-3}
0.50	4.252×10^{-1}	1.026	-1.336×10^{-1}	5.582×10^{-1}	-3.995×10^{-2}	3.286×10^{-1}	-4.637×10^{-3}
0.75	4.507×10^{-1}	1.017	-1.258×10^{-1}	5.933×10^{-1}	-4.109×10^{-2}	3.562×10^{-1}	-4.613×10^{-3}
1.00	4.716×10^{-1}	1.092	-1.378×10^{-1}	6.055×10^{-1}	-4.057×10^{-2}	3.718×10^{-1}	-4.602×10^{-3}
1.50	4.859×10^{-1}	1.053	-1.260×10^{-1}	6.367×10^{-1}	-4.277×10^{-2}	3.886×10^{-1}	-4.601×10^{-3}
2.00	4.886×10^{-1}	1.051	-1.250×10^{-1}	6.359×10^{-1}	-4.197×10^{-2}	3.932×10^{-1}	-4.625×10^{-3}
3.00	4.907×10^{-1}	9.880×10^{-1}	-1.105×10^{-1}	6.469×10^{-1}	-4.229×10^{-2}	4.021×10^{-1}	-4.627×10^{-3}
4.00	5.033×10^{-1}	1.228	-1.610×10^{-1}	6.062×10^{-1}	-3.667×10^{-2}	3.977×10^{-1}	-4.590×10^{-3}
5.00	4.986×10^{-1}	1.102	-1.340×10^{-1}	6.311×10^{-1}	-3.990×10^{-2}	4.015×10^{-1}	-4.583×10^{-3}
7.50	4.910×10^{-1}	1.049	-1.240×10^{-1}	6.579×10^{-1}	-4.578×10^{-2}	3.901×10^{-1}	-4.583×10^{-3}
10.00	4.711×10^{-1}	8.445×10^{-1}	-8.300×10^{-2}	6.848×10^{-1}	-5.105×10^{-2}	3.828×10^{-1}	-4.583×10^{-3}

GMPEs to model magnitude scaling for $\mathbf{M} > 6.0$ (hereafter referred to as the empirical-scaling approach). Figures 3 and 4 display the magnitude-scaling characteristics of the PSA predicted by our CENA GMPE for $R_{\mathrm{rup}} = 5$, 10, 30, and 70 km using the stochastic-scaling and NGA-West2 empirical-scaling approaches, respectively. These figures show that

Table 7
Coefficients of the Within-Event Variability Model in Natural Log Units

Period	C_{19}	C_{20}	C_{21}	C_{22}	C_{23}	C_{24}	C_{25}
PGA	8.376×10^{-1}	-2.941×10^{-2}	1.880	-2.610×10^{-1}	7.848×10^{-1}	-4.203×10^{-2}	5.116×10^{-1}
0.01	8.379×10^{-1}	-2.941×10^{-2}	1.879	-2.607×10^{-1}	7.849×10^{-1}	-4.194×10^{-2}	5.122×10^{-1}
0.02	8.437×10^{-1}	-3.016×10^{-2}	1.886	-2.617×10^{-1}	7.889×10^{-1}	-4.235×10^{-2}	5.135×10^{-1}
0.03	8.685×10^{-1}	-3.285×10^{-2}	1.925	-2.677×10^{-1}	8.097×10^{-1}	-4.458×10^{-2}	5.198×10^{-1}
0.04	8.865×10^{-1}	-3.425×10^{-2}	1.974	-2.759×10^{-1}	8.224×10^{-1}	-4.559×10^{-2}	5.259×10^{-1}
0.05	9.042×10^{-1}	-3.566×10^{-2}	2.022	-2.841×10^{-1}	8.346×10^{-1}	-4.660×10^{-2}	5.314×10^{-1}
0.08	9.021×10^{-1}	-3.464×10^{-2}	1.967	-2.713×10^{-1}	8.363×10^{-1}	-4.514×10^{-2}	5.425×10^{-1}
0.10	8.940×10^{-1}	-3.336×10^{-2}	1.870	-2.503×10^{-1}	8.416×10^{-1}	-4.458×10^{-2}	5.515×10^{-1}
0.15	8.847×10^{-1}	-3.049×10^{-2}	1.855	-2.460×10^{-1}	8.345×10^{-1}	-4.200×10^{-2}	5.613×10^{-1}
0.20	8.709×10^{-1}	-2.816×10^{-2}	1.770	-2.280×10^{-1}	8.313×10^{-1}	-4.022×10^{-2}	5.698×10^{-1}
0.25	8.477×10^{-1}	-2.513×10^{-2}	1.689	-2.122×10^{-1}	8.126×10^{-1}	-3.683×10^{-2}	5.732×10^{-1}
0.30	8.101×10^{-1}	-2.010×10^{-2}	1.475	-1.679×10^{-1}	8.021×10^{-1}	-3.327×10^{-2}	5.858×10^{-1}
0.40	7.563×10^{-1}	-1.369×10^{-2}	1.155	-1.022×10^{-1}	7.894×10^{-1}	-2.917×10^{-2}	5.998×10^{-1}
0.50	7.192×10^{-1}	-9.542×10^{-3}	9.129×10^{-1}	-5.258×10^{-2}	7.771×10^{-1}	-2.542×10^{-2}	6.118×10^{-1}
0.75	6.487×10^{-1}	-2.016×10^{-3}	5.115×10^{-1}	2.847×10^{-2}	7.394×10^{-1}	-1.711×10^{-2}	6.281×10^{-1}
1.00	6.028×10^{-1}	2.617×10^{-3}	3.564×10^{-1}	5.736×10^{-2}	6.813×10^{-1}	-7.617×10^{-3}	6.318×10^{-1}
1.50	5.479×10^{-1}	7.745×10^{-3}	2.408×10^{-1}	7.599×10^{-2}	5.958×10^{-1}	4.986×10^{-3}	6.282×10^{-1}
2.00	5.176×10^{-1}	1.187×10^{-2}	2.150×10^{-1}	7.910×10^{-2}	5.574×10^{-1}	1.063×10^{-2}	6.264×10^{-1}
3.00	5.156×10^{-1}	1.149×10^{-2}	2.479×10^{-1}	7.098×10^{-2}	5.505×10^{-1}	1.046×10^{-2}	6.185×10^{-1}
4.00	5.005×10^{-1}	1.287×10^{-2}	2.822×10^{-1}	6.137×10^{-2}	5.287×10^{-1}	1.208×10^{-2}	6.072×10^{-1}
5.00	4.748×10^{-1}	1.563×10^{-2}	2.037×10^{-1}	7.588×10^{-2}	5.122×10^{-1}	1.417×10^{-2}	6.043×10^{-1}
7.50	4.211×10^{-1}	2.163×10^{-2}	-1.653×10^{-2}	1.189×10^{-1}	4.920×10^{-1}	1.717×10^{-2}	6.036×10^{-1}
10.00	3.946×10^{-1}	2.512×10^{-2}	-5.540×10^{-2}	1.251×10^{-1}	4.898×10^{-1}	1.609×10^{-2}	5.944×10^{-1}

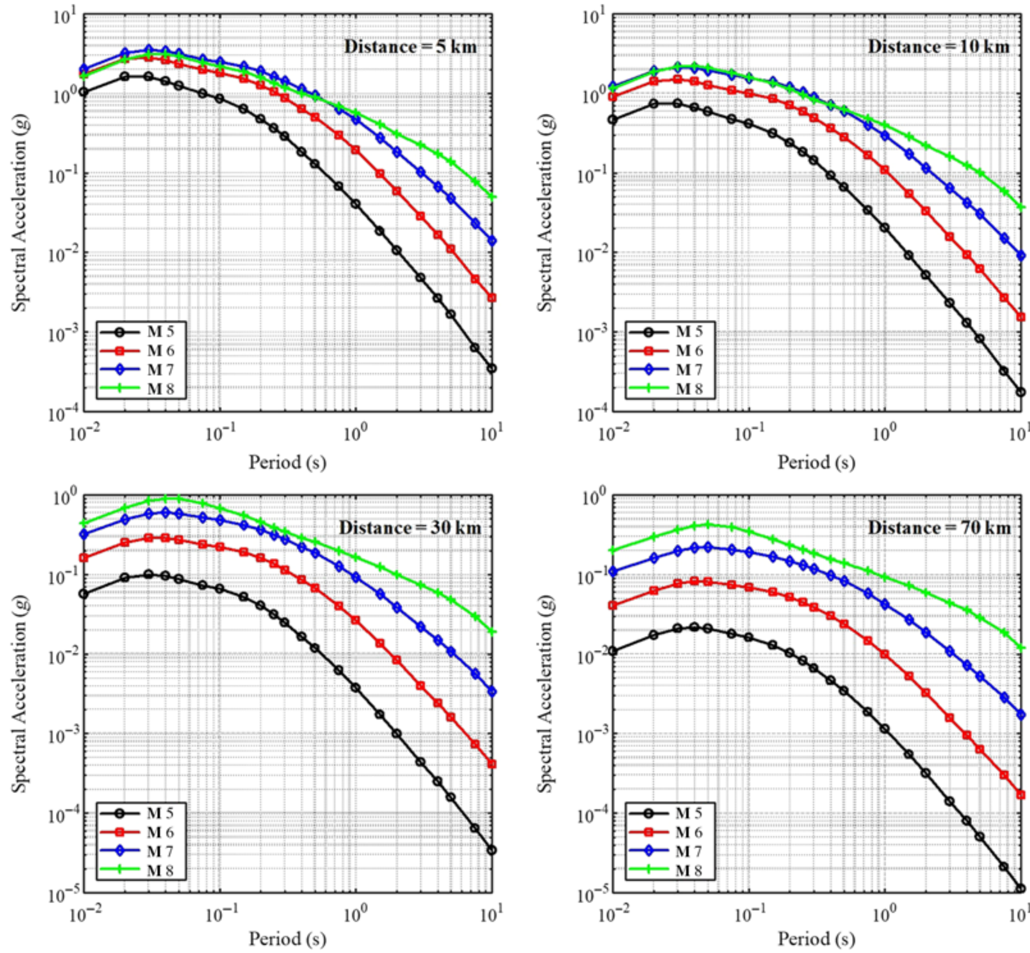

Figure 3. Response spectra predicted by the CENA hybrid empirical GMPE developed in this study based on the stochastic-scaling approach to large-magnitude scaling showing its dependence on magnitude at rupture distances ($R_{\rm rup}$) of 5, 10, 30, and 70 km. The color version of this figure is available only in the electronic edition.

the empirical-scaling approach does not exhibit as much oversaturation at large magnitudes, short distances, and short periods as the stochastic-scaling approach. Because the consensus among engineering seismologists is to preclude oversaturation in GMPEs (e.g., see ASK14 and CB14), we prefer the version of the CENA GMPE that is based on the empirical-scaling approach.

Comparison with Previous Models

Figure 5 shows a comparison of the distance-scaling (attenuation) characteristics of the GMPEs developed in this study (hereafter, PZCT14) with those of Pezeshk *et al.* (2011; hereafter, PZT11) and the hard-rock version of Campbell (2007, 2008, 2011; hereafter, C07). Plots are shown for PGA and PSA at $T = 0.1$, 0.2, 0.5, 1.0, and 4.0 s, **M** 5.0 and 7.0, and $R_{\rm rup} = 1$–500 km. Our models were developed for distances up to 1000 km, but here we used 500 km for plotting purposes. Both C07 and PZT11 used the HEM approach to develop GMPEs for the generic CENA hard-rock site conditions defined by Atkinson and Boore (2006), which correspond to NEHRP site class A (BSSC, 2009) with $V_{S30} \geq 2000$ m/s and $\kappa_0 = 0.005$ s. To perform a consistent comparison, the estimated GMIMs from C07 and PZT11 were adjusted to the reference hard-rock site conditions used in this study, which corresponds to $V_{S30} = 3000$ m/s and $\kappa_0 = 0.006$ s (Hashash, Kottke, Stewart, Campbell, Kim, Moss, *et al.*, 2014). This adjustment was approximated by multiplying the C07 and PZT11 GMIM predictions by the ratio of the site-amplification factors in Atkinson and Boore (2006) to those used in this study (Boore and Thompson, 2015). No adjustment for κ_0 was done because we believe that the value of 0.005 s used by C07 and PZT11 and the value of 0.006 s used in this study leads to negligible differences in site attenuation for the frequencies of interest in this study.

PZT11 used a lower median stress parameter for CENA compared with this study (250 vs. 400 bars).

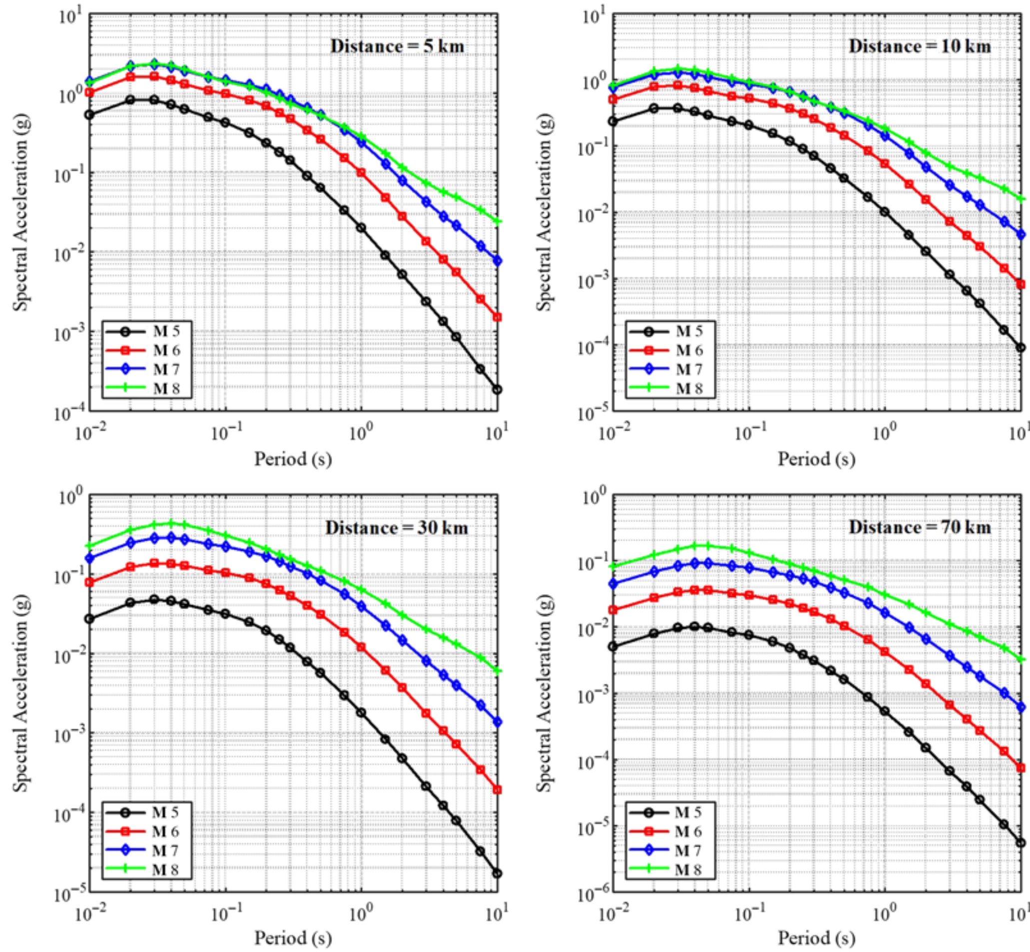

Figure 4. Response spectra predicted by the CENA hybrid empirical GMPE developed in this study based on the empirical-scaling approach to large-magnitude scaling showing its dependence on magnitude at rupture distances (R_{rup}) of 5, 10, 30, and 70 km. The color version of this figure is available only in the electronic edition.

Similarly, C07 used a stress parameter of 280 bars. Although this appears to be inconsistent, we note that these lower stress parameters are consistent with the value of 250 bars found by Boore (2009) and Atkinson *et al.* (2009) to approximate the finite-fault predictions of Atkinson and Boore (2006), based on a stress parameter of 140 bars, using the point-source stochastic simulation program SMSIM. Because all of these models are calibrated with CENA recordings, the differences in the stress parameters are self-consistent and do not represent a bias in the GMIM predictions. From Figure 5, we observe that the GMIM predictions of C07 and PZT11 are similar to the predictions of this study at high frequencies for **M** 5.0 and $R_{rup} > 10$ km; however, they are generally smaller for **M** 7.0. One important difference at short distances is the use of the new effective point-source distance metric defined in equation (3) that was used to model the near-source magnitude-saturation effects in the stochastic-scaling approach. The use of this distance metric clearly leads to greater saturation (in fact, oversaturation) at short periods, short distances, and large magnitudes compared with the empirical-scaling approach. PZT11 used a similar effective distance metric, but C07 did not (Campbell, 2014). For longer periods, the C07 and PZT11 predictions are smaller even for **M** 5.0 and $R_{rup} > 10$ km.

Youngs and Kuehn (2015) extrapolated NGA-East models including Pezeshk *et al.* (2015) GMM at close and/or large distances to cover the full range of R_{rup} (0–1500 km). They extrapolated values so that the value at 1000 km predicted by the fitted model matched the value provided by Pezeshk *et al.* (2015) and this study. Youngs and Kuehn (2015) applied adjustment factor for close distances to prevent oversaturation. They achieved this as follows: “for each frequency, the magnitude curve that produced the highest ground motions at $R_{rup} = 0$ is identified as the upper-limit ground motions. Then, starting in sequence with the next highest magnitude, the ground motions at each distance are taken to be the maximum of the values for that magnitude and the magnitude below. In this way, full saturation is achieved.” (p. 19).

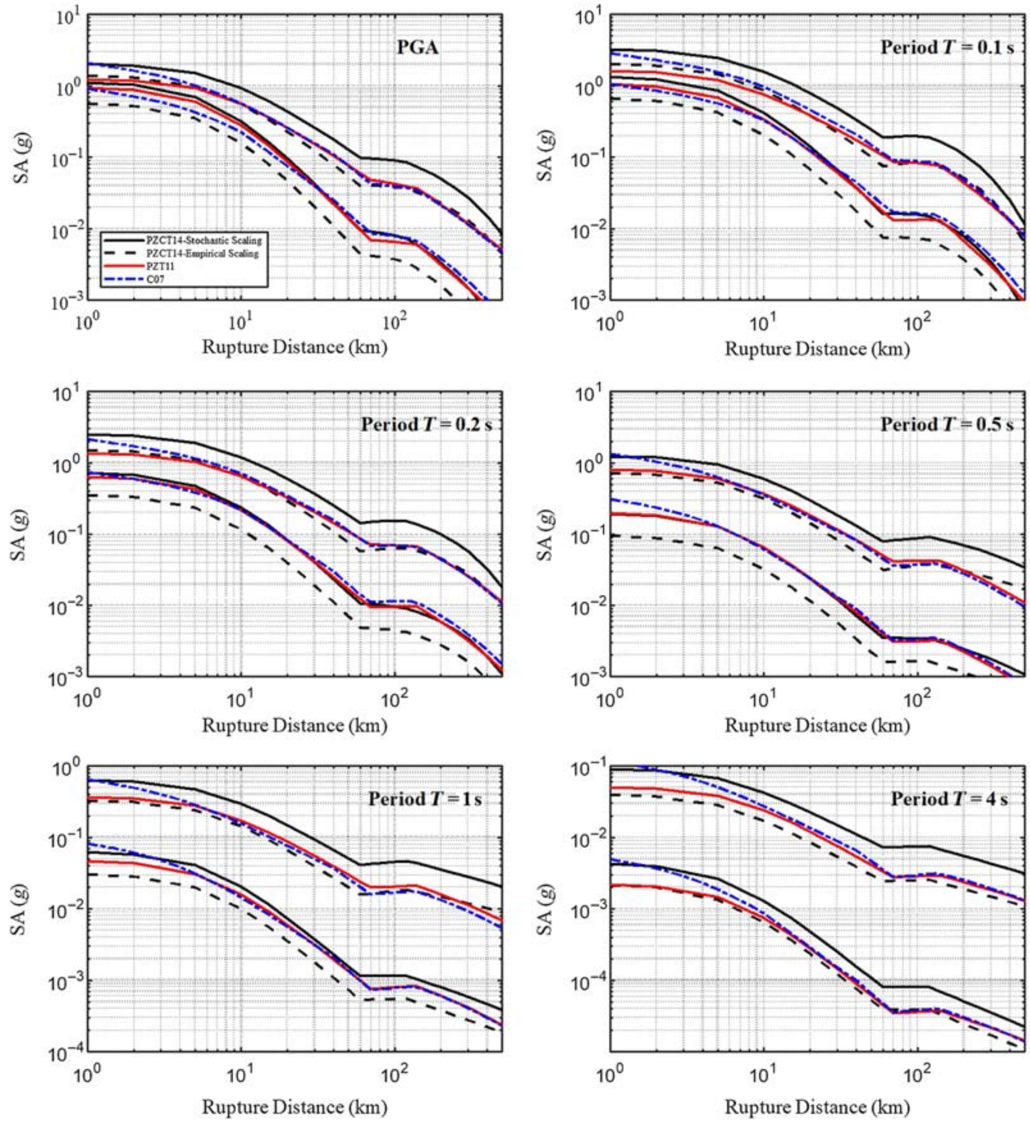

Figure 5. Comparison of peak ground acceleration (PGA) and pseudoacceleration response spectral acceleration (PSA) predicted by the CENA GMPEs developed in this study (PZCT14) with the predictions of two hybrid empirical models developed previously by the authors: (lower curve) **M** 5; (upper curve) **M** 7; PZT11, Pezeshk *et al.* (2011); C07, Campbell (2007, 2008, 2011); SA, spectral acceleration. The color version of this figure is available only in the electronic edition.

Comparison with Observations

The GMIM predictions from the GMPEs developed in this study are compared with the PGA and PSA values from the NGA-East database (Goulet *et al.*, 2014; see Data and Resources) for available CENA recordings with $\mathbf{M} \geq 4.0$ and $R_{\mathrm{rup}} < 1000$ km. For this comparison, we only use tectonic earthquakes and not the potentially induced events (PIEs) identified in the NGA-East database (Goulet *et al.*, 2014) because of the scientific controversy about whether PIEs have different source or attenuation characteristics than tectonic events (e.g., Hough, 2014). We used the RotD50 horizontal GMIMs that are listed in the database to be consistent with the definition of the GMIMs used in the NGA-West2 GMPEs. We excluded earthquakes and recording stations in the Gulf Coast region, which has been shown to exhibit significantly different ground-motion attenuation because of the thick sediments in the region (Dreiling *et al.*, 2014). Figure 6 displays a map of the recording stations with different shades representing their NEHRP site class, and Figure 7 displays a map of the associated earthquakes. NEHRP site class E (soft-soil) sites were excluded from consideration because of their complex site-response characteristics and their potential for significant nonlinear site effects. Figure 8 displays the magnitude–distance distribution of the selected recordings.

As seen in Figure 6, the selected recordings were obtained on a variety of site conditions. To perform a consistent

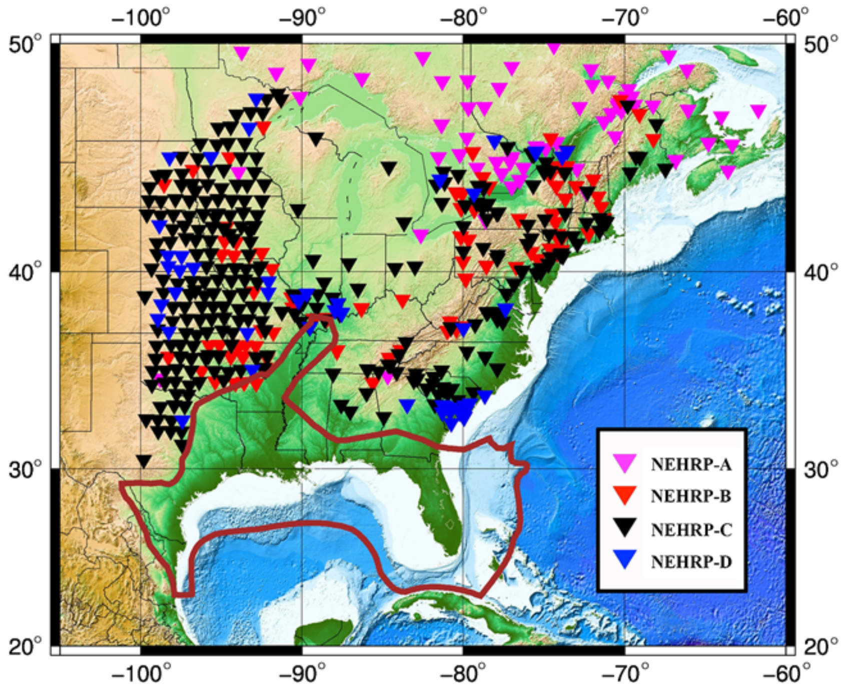

Figure 6. CENA recording stations used in the comparisons with the hybrid empirical GMPE developed in this study. All stations located within Gulf Coast region were excluded. NEHRP, National Earthquake Hazards Reduction Program. The color version of this figure is available only in the electronic edition.

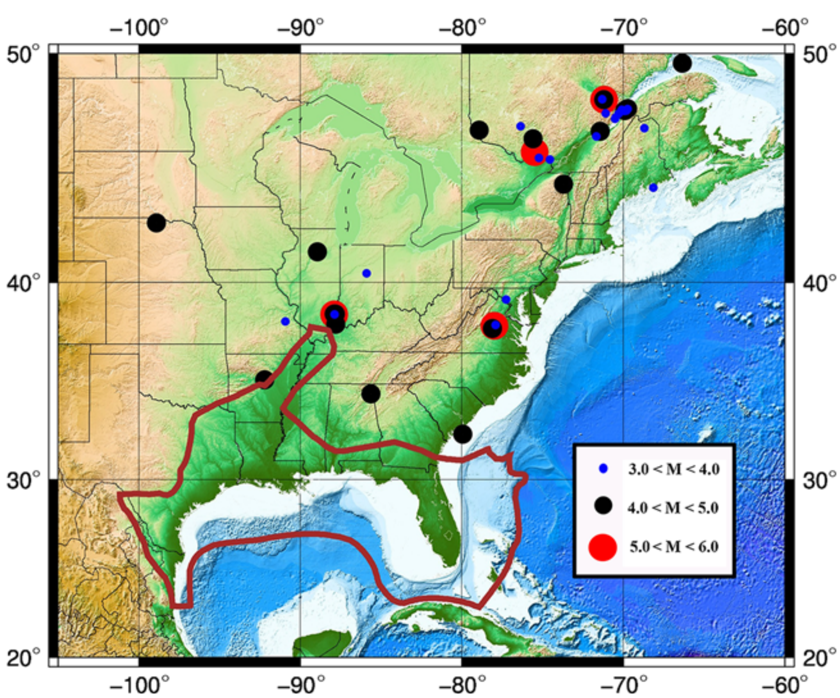

Figure 7. CENA earthquakes used in the comparisons with the hybrid empirical GMPE developed in this study. All potentially induced earthquakes (PIEs) and events located within the Gulf Coast region were excluded. The color version of this figure is available only in the electronic edition.

comparison between the GMIM predictions from the GMPE developed in this study and the observations, the observed GMIMs were adjusted to the CENA hard-rock reference site condition used to develop the GMPE based on the same approach used in the NGA-East project (C. A. Goulet, personal comm., 2014). We first adjusted the observed PSA and PGA values for sites with $V_{S30} < 1500$ m/s to NEHRP B/C site conditions ($V_{S30} = 760$ m/s) using the site term in BSSA14. This site term is a function of V_{S30} and PGA_R, the median value of PGA on NEHRP B/C site conditions. The BSSA14 site term includes two parts: a linear term F_{LIN} that is a function of V_{S30} only and a nonlinear term F_{NL} that is a function of both V_{S30} and PGA_R. To avoid an iterative process, an estimate of PGA_R for each recording was obtained from a point-source stochastic simulation for each magnitude, distance, and spectral period of interest using the CENA seismological parameters given in Table 2 and then adjusted to CENA hard-rock site conditions using the crustal-amplification factors for a generic CENA NEHRP B/C site from table 4 of Atkinson and Boore (2006). After adjusting the observed GMIM values to the NEHRP B/C site conditions, we used the spectral crustal-amplification factors in table 4 of Atkinson and Boore (2006) to adjust the GMIMs to CENA hard-rock site conditions. The hard-rock sites with $V_{S30} \geq 1500$ m/s were adjusted to $V_{S30} = 3000$ m/s using a different method, as discussed in the next paragraph.

A summary of the method that we used to adjust the observations to the CENA reference hard-rock site condition can be described as follows (similar to the Boore and Campbell, 2017, approach):

1. Compile generic V_S and density profiles corresponding to $V_{S30} = 760$ m/s (Atkinson and Boore, 2006), $V_{S30} = 2000$ m/s (Atkinson and Boore, 2006), and $V_{S30} = 3000$ m/s (Boore and Thompson, 2015).
2. For each recording of given **M**, R_{rup}, and $V_{S30} < 1500$ m/s, correct to $V_{S30} = 760$ m/s using the site term in BSSA14 and the value of PGA_R from the CENA stochastic simulations after correcting to NEHRP B/C site

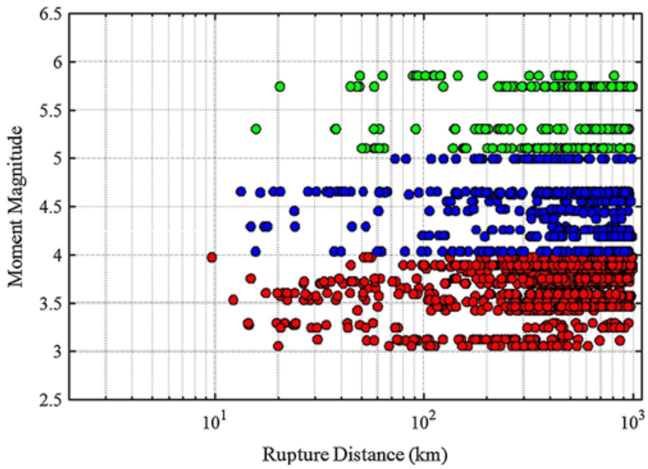

Figure 8. The magnitude–distance distribution of the selected CENA ground-motion recordings used to compare with the hybrid empirical GMPE developed in this study. All PIEs and events located within the Gulf Coast region were excluded. The color version of this figure is available only in the electronic edition.

conditions using the ratio of the crustal-amplification factors for the $V_{S30} = 760$ and 3000 m/s site profiles. For the few sites with $1500 < V_{S30} < 2000$ m/s, stochastically simulate the value of PGA and PSA using the crustal-amplification factors for the $V_{S30} = 2000$ m/s site profile.

3. Find the ratio of PGA and PSA values between the $V_{S30} = 760$ and 3000 m/s site profiles or between the $V_{S30} = 2000$ and 3000 m/s site profiles and use these as adjustment factors to correct the recorded GMIM values to the reference hard-rock site conditions.

Figure 9 compares the site factors that were used to adjust the observed PSA values from the reference NEHRP B/C site condition, or alternatively from the Atkinson and Boore (2006) hard-rock site condition, to the CENA reference hard-rock site condition, which includes the effects of both crustal amplification and site attenuation. The plots show the spectral ratio of PSA between the 3000 m/s and 3000 m/s site profiles (Fig. 9a) and between the $V_{S30} =$ 2000 and 3000 m/s site profiles (Fig. 9b). Ratios are given for **M** 3.5, 4.5, 5.5, and 6.5, and $R_{\mathrm{rup}} = 10$ and 100 km. The magnitude range was selected to show the adjustment factors that are most relevant to the magnitudes of the observed earthquakes. The two distances are provided to demonstrate how the adjustment factors vary with distance. These plots show that the adjustments can be relatively large for the NEHRP B/C site profile and almost negligible for the $V_{S30} =$ 2000 m/s site profile.

Figure 10 compares the median predicted values of PSA from the GMPE based on stochastic scaling at large magnitudes versus the site-adjusted observed PSA at $T = 0.2$, 1.0, and 2.0 s for three one-unit magnitude bins centered at **M** 3.5, 4.5, and 5.5. These comparisons include the common log empirical calibration constant of 0.32 (factor of 2.09) that was used to adjust the GMIM predictions from the GMPE for the average misfit between the predictions and the observations over all magnitudes, distances, and spectral periods. In general, there is relatively a good agreement between the PSA predictions and the observations, although there are some magnitudes and distances where the comparison is better than others. We note that there is a great deal of uncertainty associated with adjusting the observed GMIMs to the reference hard-rock site conditions in CENA that precludes making definitive conclusions regarding their comparison with the predicted values.

Figure 11 shows the total residuals from the GMIM predictions that are based on stochastic scaling at large magnitudes as a function of distance for $T = 0.2$, 1.0, and 2.0 s. In this figure, the size of each circle and its shades represents the magnitude of the earthquake. Squares represent the mean values and the error bars represent the 95th percentile confidence limits of the mean of the binned residuals. This figure shows that there is about a 50% statistically significant underestimation by the GMPE for binned distances ranging from 50 to 300 km, but this underestimation disappears at longer periods (lower frequencies). Otherwise there is no substantial trend in the total residuals with distance.

A variance-component technique proposed by Chen and Tsai (2002) was used to decompose the prediction error of the GMIMs into three components, which using the terminology of Al Atik *et al.* (2010), are (1) the between-event standard deviation τ, (2) the site-to-site standard deviation ϕ_{S2S}, and (3) the within-event single-site standard deviation ϕ_{SS}. Figure 12 displays these residuals for $T = 1.0$ s as a function of magnitude and distance. As can be seen in this figure, the total residual errors are significantly reduced after they are corrected for the between-event and the site-to-site components of variability. This difference can be seen even more clearly in Table 8, which lists the natural log standard deviations of the three components of variability for PSA at $T = 0.2$, 1.0, and 2.0 s. The standard deviations in this table are given in natural log units so that they can be compared more easily with the standard deviations listed in the literature as well as those recommended in this study for use with our GMPE (see equations 6 and 7 and the coefficients listed in Tables 6 and 7).

Table 8 compares the natural log standard deviations of the between-event variability (τ) and the within-event variability (ϕ) estimated from the CENA observations with those recommended in this study for an **M** 4.0 event. This magnitude was selected because it is near the average of the magnitudes of the observed events. The within-event standard deviation of the observations was calculated from the SRSS of ϕ_{S2S} and ϕ_{SS}. The values of τ from the observations are found to be similar to or even somewhat smaller than those from the GMPE aleatory variability model. However, the values of ϕ from the observations are generally higher, likely because of the additional dispersion that results from

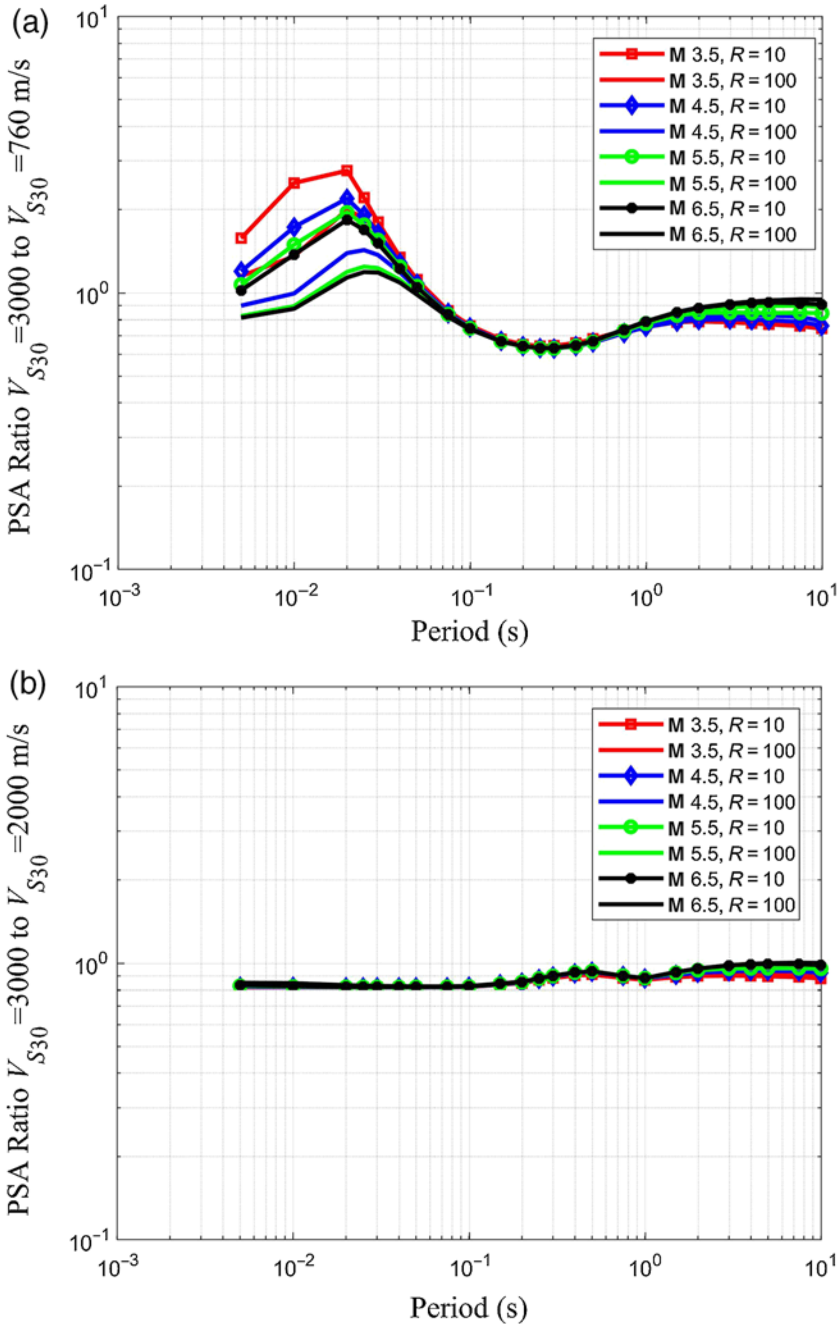

Figure 9. Comparisons of (a) the $V_{S30} = 3000$ m/s to NEHRP B/C ($V_{S30} = 760$ m/s) PSA spectral ratios and (b) the $V_{S30} = 3000$ to 2000 m/s PSA spectral ratios used to adjust the empirical observations to the CENA reference hard-rock site condition recommended by Hashash, Kottke, Stewart, Campbell, Kim, Moss, *et al.* (2014). The color version of this figure is available only in the electronic edition.

the large site adjustment and the uncertainty whether the BSSA14 site term is appropriate in CENA. The result is that the total standard deviation (σ) is somewhat larger for the observations than for the GMPE aleatory variability model. It is also interesting to compare the within-event and single-site standard deviations of the observations with those summarized in Rodriguez-Marek *et al.* (2013) for different tectonic regions. The values of ϕ and ϕ_{SS} tend to fall in the upper range of the values shown in figure 2 of Rodriguez-Marek *et al.* (2013). This is not surprising considering the relatively large amount of uncertainty associated with the large site adjustment that was applied to the observed GMIMs. Interestingly, the standard deviations from the observations are similar to those found by Rodriguez-Marek *et al.* (2013) for California, which were derived from events dominated by the same magnitude range as the CENA events.

Figure 13 compares response spectra from our two proposed GMPEs (PZCT-M1SS and PZCT-M2ES) with the other NGA-East GMPEs (PEER, 2015), which include B-a04, B-ab14, B-ab95, B-bca10d, B-s11, B-sgd02, 1CCSP, 1CVSP, 2CCSP, 2CVSP, YA15, Frankel, and HA15. In addition, we include the more recent GMPEs of Graizer (2016; hereafter, G16) and Shahjouei and Pezeshk (2016; hereafter, SP16) models in this and subsequent comparisons, which we refer to as CENA GMPEs for brevity. The spectral accelerations are shown for an earthquake magnitude of **M** 5 and 7 for rupture distances of 10, 30, 70, and 100 km at spectral accelerations ranging from 0.1 to 100 Hz (periods of 0.01 to 10 s). For comparison purposes, the Joyner–Boore distances used in SP16 were converted to equivalent rupture distances using the Scherbaum *et al.* (2004) magnitude–distance conversion relation. Figure 14 shows the attenuation of spectral accelerations at frequencies 0.5, 1.0, and 2.0 Hz (periods of 0.5, 1.0, and 2.0 s) for earthquake magnitudes of **M** 5 and 7 and distances up to 1000 km. Figure 15 shows how the GMPEs compare in terms of magnitude scaling for frequencies 0.5, 1.0, and 2.0 Hz and distances of 10, 100, and 400 km. Because of significant overlap of predicted spectral accelerations in Figure 15 at the higher frequencies, our proposed GMPEs (PZCT-M1SS and PZCT-M2ES) are compared with the geometric mean and $\pm 1\sigma$ of the CENA GMPEs. Figures 13–15 illustrate that our GMPEs are in good agreement with the other CENA GMPEs except for large distances in which our GMPEs have a lower predicted attenuation.

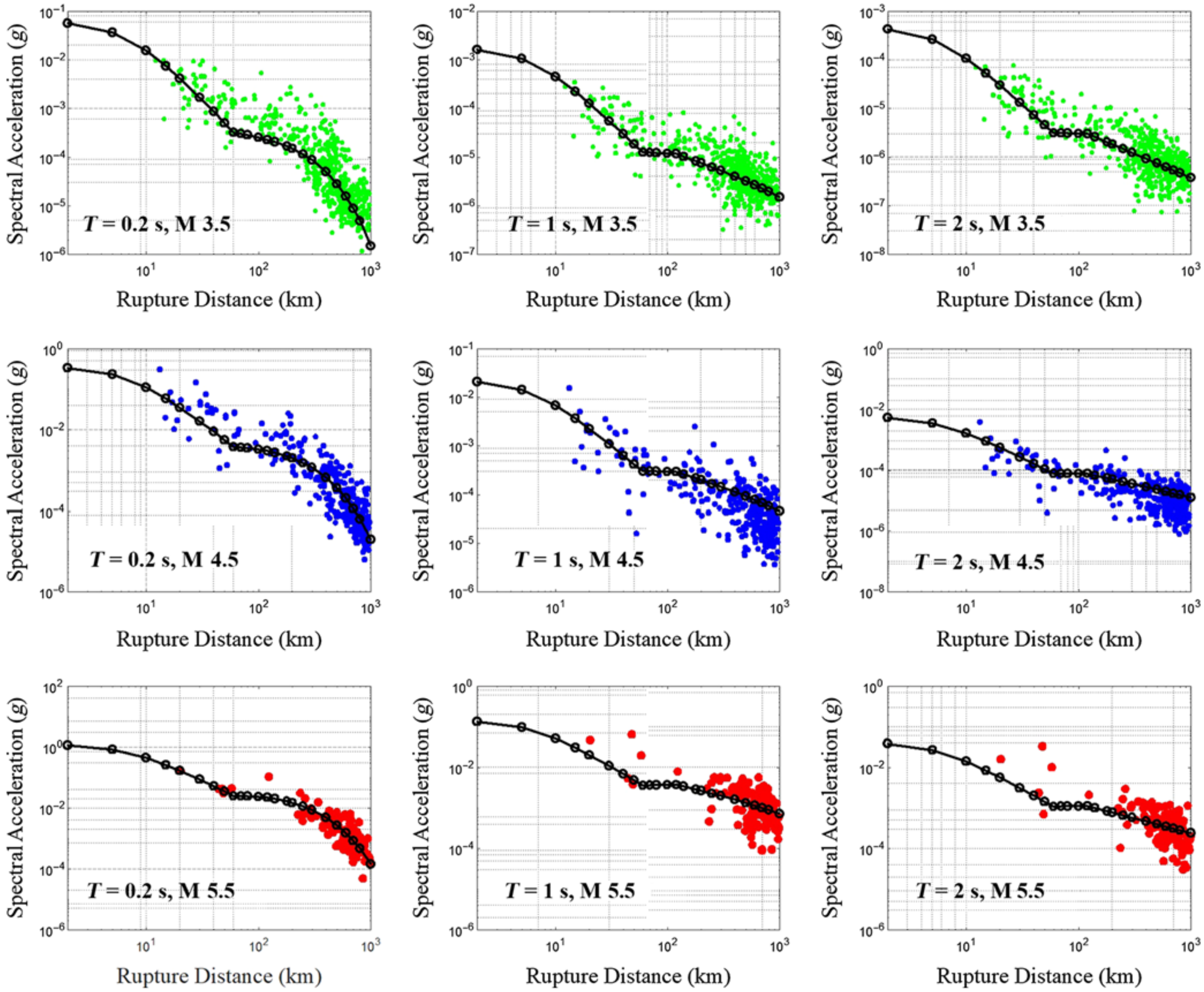

Figure 10. Comparisons of the ground-motion intensity measure (GMIM) predictions from the hybrid empirical GMPE developed in this study with the site-adjusted GMIM observations for spectral periods of 0.2, 1.0, and 2.0 s and three magnitude bins: **M** 3.5 (3.0–4.0), **M** 4.5 (4.0–5.0), and **M** 5.5 (5.0–6.0). The color version of this figure is available only in the electronic edition.

Summary and Conclusions

The HEM of Campbell (2003) was used to develop two new GMPEs for CENA. These GMPEs are based on two alternative large magnitude-scaling approaches: (1) using HEM-based GMIMs predictions for all magnitudes even though the stochastic simulations used to perform the regional adjustments were based only on seismological models that were constrained by data with $\mathbf{M} \leq 6.0$, referred to as the stochastic-scaling (PZCT-1SS) approach, and (2) using HEM-based GMIM predictions for $\mathbf{M} \leq 6.0$ and the magnitude-scaling predicted by the NGA-West2 GMPEs for larger magnitudes, referred to as the empirical-scaling (PZCT-2ES) approach. The empirical-scaling approach eliminates or significantly reduces oversaturation of GMIM predictions at large magnitudes, short distances, and short periods and is therefore preferred over the stochastic-scaling approach. The new GMPEs are valid for predicting PGA and 5% damped PSA for $T = 0.01$–10 s, **M** 4.0–8.0, and nominally for $R_{\mathrm{rup}} < 1000$ km. However, because the developers of the NGA-West2 GMPEs suggest that their models are mostly constrained by data at distances within about 300 km, we suggest that the GMIM predictions from our new GMPEs become less reliable at $R_{\mathrm{rup}} > 300$–400 km and should be used with caution at these larger distances. The GMIM predictions represent the reference CENA hard-rock site condition recommended by Hashash, Kottke, Stewart, Campbell, Kim, Moss, *et al.* (2014), which corresponds to a site with $V_{S30} = 3000$ m/s and $\kappa_0 = 0.006$ s. The prediction of GMIMs for other site conditions requires using appropriate

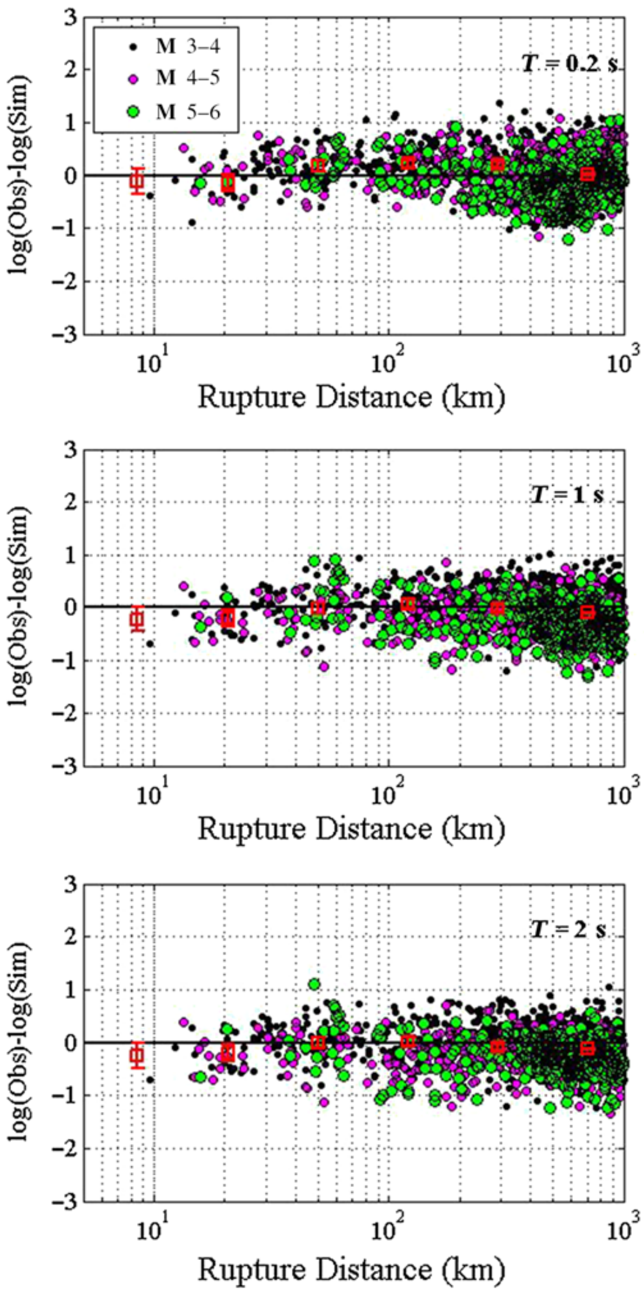

Figure 11. Plots showing the distribution of the site-adjusted residuals as a function of rupture distance (R_{rup}). The size of each circle and its shades represent the magnitude of the event. Squares represent the mean of the binned residuals. The color version of this figure is available only in the electronic edition.

site-amplification factors, such as those used to adjust the CENA recordings to the CENA reference hard-rock site condition in this study. We consider our new GMPE to be a viable alternative to both the existing set of CENA GMPEs, such as those used by Petersen *et al.* (2008) in the development of the national seismic hazard model, and to other GMPEs that have been developed as part of the NGA-East project. Including a GMPE developed using the HEM approach will be an important contribution to the distribution of epistemic uncertainty of GMIM predictions in CENA.

The application of the HEM approach in this study used WNA empirical GMPEs developed as part of the NGA-West2 project (Bozorgnia *et al.*, 2014) to estimate GMIMs in the host region. These GMPEs were evaluated for a reference firm-rock site condition corresponding to $V_{S30} = 760$ m/s and the default earthquake depths and basin effects recommended by the GMPE developers. For the WNA stochastic simulations, we used a consistent set of seismological parameters that were derived from the NGA-West2 GMPEs. For the CENA stochastic simulations, we used an updated set of regionally consistent seismological parameters that were derived by Chapman *et al.* (2014); Hashash, Kottke, Stewart, Campbell, Kim, Moss, *et al.* (2014); Boore and Thompson (2015); and Yenier and Atkinson (2015a). The major assumption in the HEM approach is that the near-source scaling and saturation effects observed in active tectonic regions, such as WNA, is a general behavior that can be extended to other tectonic regions, such as CENA. The empirical GMIM predictions from the host region were adjusted by stochastically simulated GMIM ratios that account for the differences in the source, path, and site response between the target (CENA) and the host (WNA) regions. These adjustment factors were evaluated using a point-source stochastic model with an effective point-source distance metric that mimics the distance from a finite-fault rupture plane, such as that used in the NGA-West2 GMPEs.

We used a stress parameter of 400 bars estimated by Boore and Thompson (2015), a path-duration model derived by Boore and Thompson (2014), and an attenuation model developed by Chapman *et al.* (2014) for the CENA stochastic ground-motion simulations. For WNA, all of the seismological parameters, except for κ_0, were based on the point-source inversions of the median predictions of PGA and PSA from the NGA-West2 GMPEs performed for events with $\mathbf{M} \leq 6.0$ and sites with $R_{\mathrm{rup}} < 200$ km. The value of κ_0 was derived from the NGA-West2 GMPEs using the IRVT approach of Al Atik *et al.* (2014) and fixed in the inversion to avoid a trade-off between $\Delta\sigma$ and κ_0. An effective point-source distance metric that combines those proposed by Atkinson and Silva (2000) and Yenier and Atkinson (2014, 2015a,b) was used in the stochastic simulations in both regions to capture near-source finite-fault geometric attenuation effects.

The GMIM predictions from the GMPEs developed in this study were compared with the observed GMIM values from the NGA-East database (Goulet *et al.*, 2014; see Data and Resources) by evaluating the residuals between the predictions and the observations, after adjusting the latter to the CENA reference hard-rock site condition (Hashash, Kottke, Stewart, Campbell, Kim, Moss, *et al.*, 2014). In general, there is relatively good agreement between the GMPEs and the CENA observations. We consider any

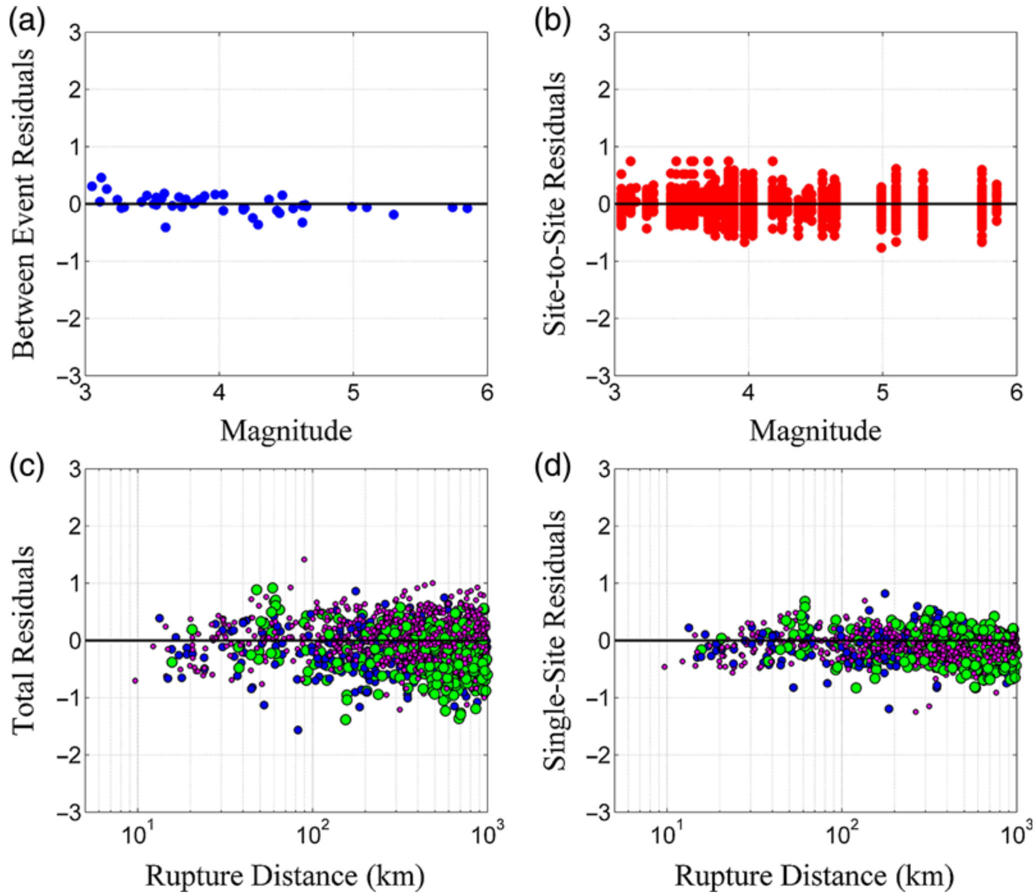

Figure 12. Plots showing (a) the between-event residuals versus magnitude, (b) the within-event residuals versus magnitude, (c) the total residuals versus rupture distance, and (d) the within-event single-site residuals versus rupture distance for a spectral period of 1.0 s. The size of each circle and its shades represent the magnitude of the event. The color version of this figure is available only in the electronic edition.

disagreement between the predictions and site-adjusted observations to be acceptable, considering the relatively large adjustments and associated uncertainty that was necessary to adjust the observations to the CENA reference hard-rock site condition. A comparison between our new GMPEs with those developed previously by the authors shows that they closely agree at **M** 5 and short periods but predict lower GMIMs at larger magnitudes and longer periods.

Table 8
Standard Deviations Segregated by Variance Components in Natural Log Units

	Period (s)					
	Observations			GMPE (M 4.0)		
Component of Variability	0.2	1.0	2.0	0.2	1.0	2.0
Between-event (τ)	0.357	0.350	0.334	0.396	0.472	0.489
Site-to-site (ϕ_{S2S})	0.668	0.596	0.484	—	—	—
Single-site (ϕ_{SS})	0.490	0.527	0.550	—	—	—
Within-event (ϕ)	0.829	0.796	0.733	0.752	0.703	0.560
Total (σ)	0.902	0.870	0.805	0.850	0.846	0.743

GMPE, ground-motion prediction equation.

Data and Resources

We used the peak ground acceleration (PGA) and response spectra of central and eastern North America (CENA)–recorded ground motions and related metadata that were compiled and processed by the Next Generation Attenuation-East (NGA-East) project and provided to us by Christine A. Goulet in the form of a flatfile. All of the other data and models used in this study are available in the References.

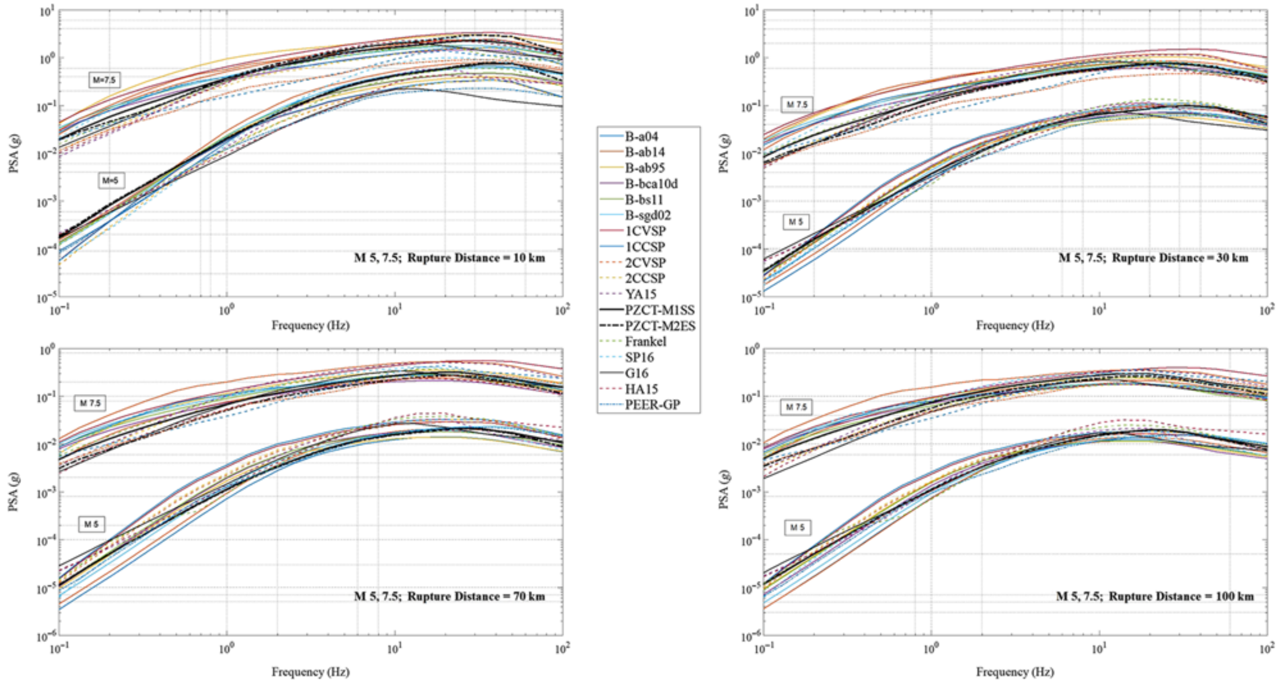

Figure 13. Comparison of predicted spectral accelerations for the two GMPEs proposed in this study (PZCT-M1SS and PZCT-M2ES) with those developed recently for CENA for an earthquake magnitude of **M** 5 and 7.5 for rupture distances of 10, 30, 70, and 100 km. See the Comparison with Observations section for a description of the GMPEs. The color version of this figure is available only in the electronic edition.

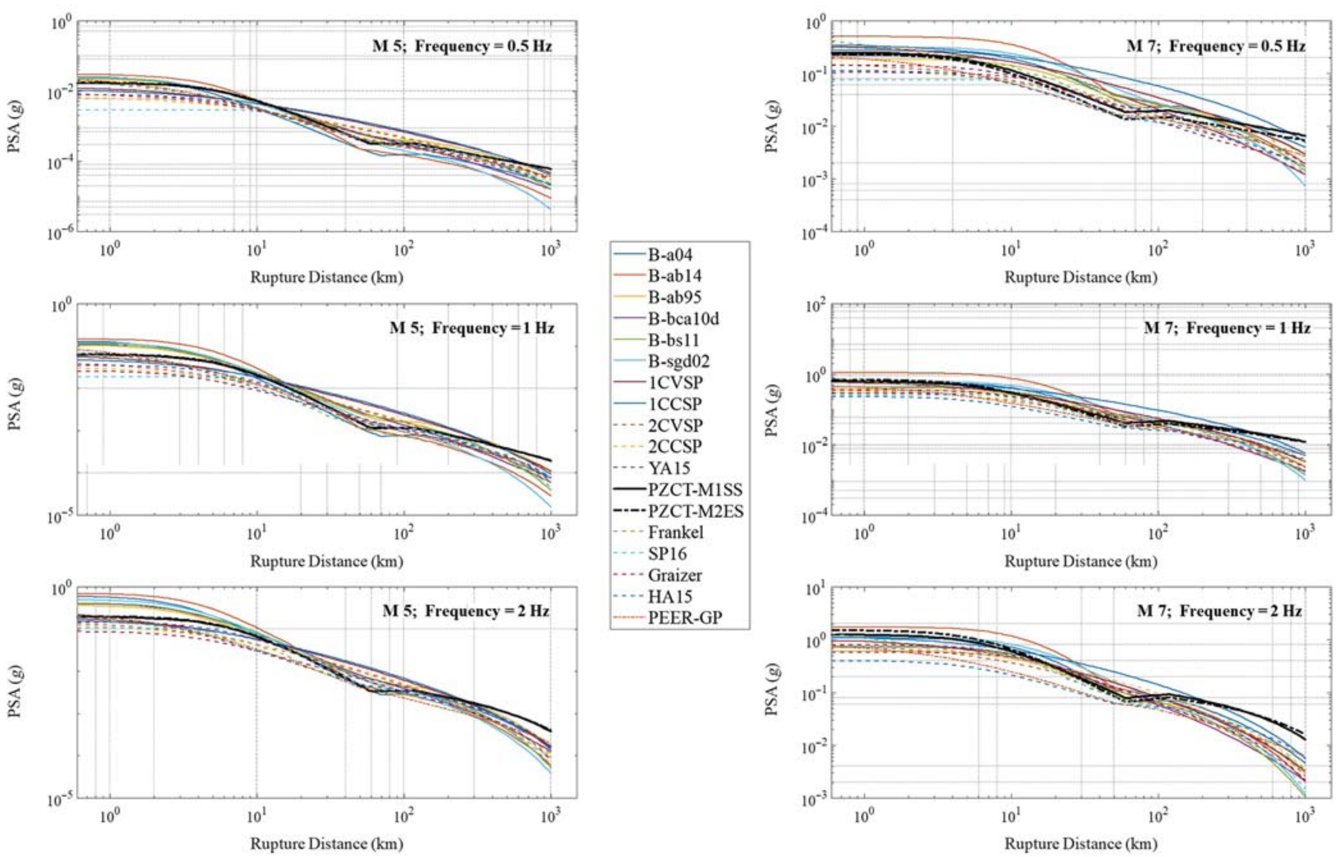

Figure 14. Comparison of predicted attenuation of spectral accelerations for the GMPEs proposed in this study (PZCT-M1SS and PZCT-M2ES) with those developed recently for CENA at frequencies 0.5, 1, and 2 Hz for earthquake magnitudes of **M** 5 and 7 and rupture distances up to 1000 km. See the Comparison with Observations section for a description of the GMPEs. The color version of this figure is available only in the electronic edition.

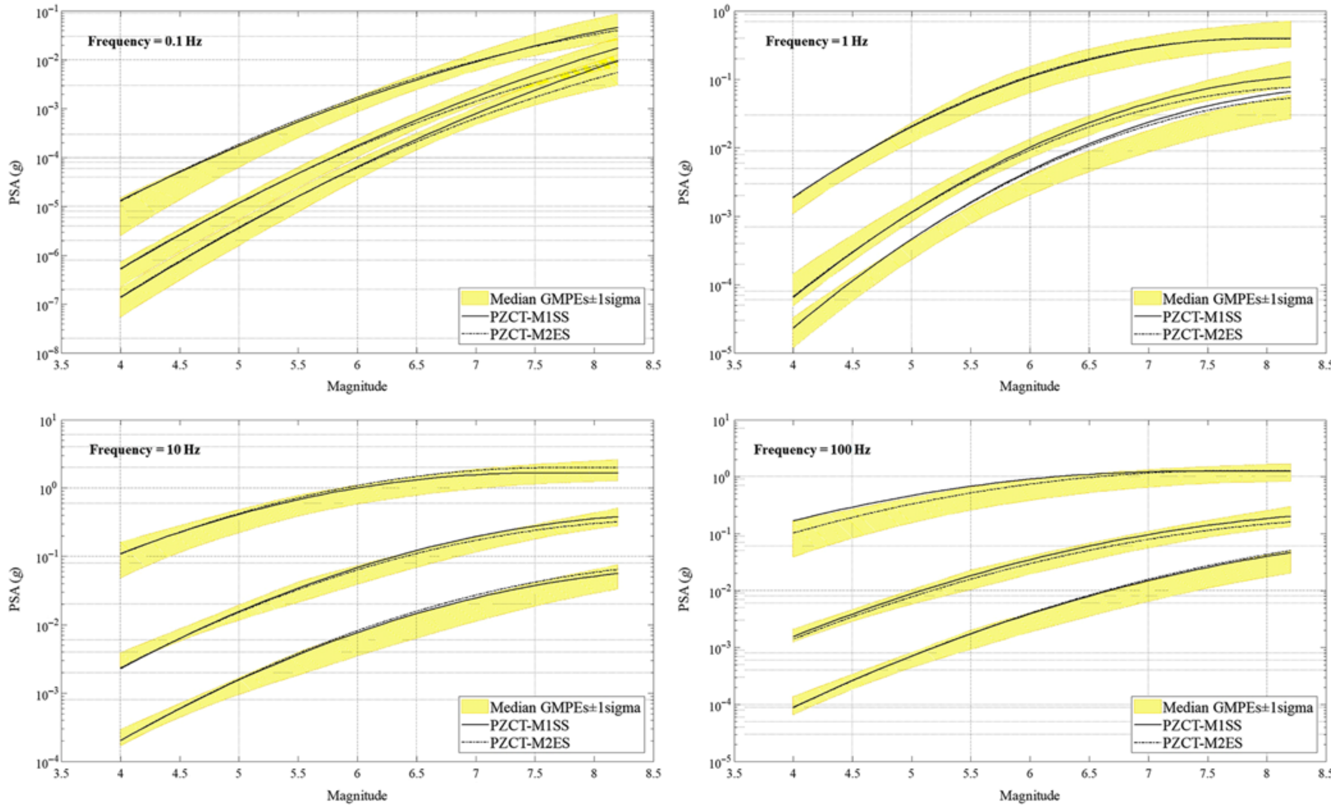

Figure 15. Comparison of magnitude scaling of spectral accelerations for the GMPEs proposed in this study (PZCT-M1SS and PZCT-M2ES) with the geometric mean and 95% confidence interval (CI) of those GMPEs developed recently for CENA at frequencies 0.1, 1, 10, and 100 Hz and distances of 10, 100, and 400 km. See the Comparison with Observations section for a description of the GMPEs. The color version of this figure is available only in the electronic edition.

Acknowledgments

The authors would like to thank Christine Goulet, Norm Abrahamson, and Alireza Haji-Soltani for their insightful comments and suggestions, which greatly improved the article. The authors would also like to thank Trevor Allen and an anonymous reviewer for their comments and review of this article.

References

Abrahamson, N. A., W. J. Silva, and R. Kamai (2014). Summary of the ASK14 ground motion relation for active crustal regions, *Earthq. Spectra* **30,** 1025–1055.

Al Atik, L., and R. R. Youngs (2014). Epistemic uncertainty for NGA-West2 models, *Earthq. Spectra* **30,** 1301–1318.

Al Atik, L., N. Abrahamson, J. J. Bommer, F. Scherbaum, F. Cotton, and N. Kuehn (2010). The variability of ground-motion prediction models and its components, *Seismol. Res. Lett.* **81,** 794–801.

Al Atik, L., A. Kottke, N. A. Abrahamson, and J. Hollenback (2014). Kappa (κ) scaling of ground-motion prediction equations using an inverse random vibration theory approach, *Bull. Seismol. Soc. Am.* **104,** 336–346.

Anderson, J. G., and S. E. Hough (1984). A model for the shape of the Fourier amplitude spectrum of acceleration at high frequencies, *Bull. Seismol. Soc. Am.* **74,** 1969–1993.

Atkinson, G. M. (2004). Empirical attenuation of ground motion spectral amplitudes in southeastern Canada and the northeastern United States, *Bull. Seismol. Soc. Am.* **94,** 1079–1095.

Atkinson, G. M., and K. Assatourians (2010). Attenuation and source characteristics of the 23 June 2010 M 5.0 Val-des-Bois, Quebec, earthquake, *Seismol. Res. Lett.* **81,** 849–860.

Atkinson, G. M., and D. M. Boore (1995). New ground motion relations for eastern North America, *Bull. Seismol. Soc. Am.* **85,** 17–30.

Atkinson, G. M., and D. M. Boore (1998). Evaluation of models for earthquake source spectra in eastern North America, *Bull. Seismol. Soc. Am.* **88,** 917–934.

Atkinson, G. M., and D. M. Boore (2006). Ground motion prediction equations for earthquakes in eastern North America, *Bull. Seismol. Soc. Am.* **96,** 2181–2205.

Atkinson, G. M., and D. M. Boore (2011). Modifications to existing ground-motion prediction equations in light of new data, *Bull. Seismol. Soc. Am.* **101,** 1121–1135.

Atkinson, G. M., and D. M. Boore (2014). The attenuation of Fourier amplitudes for rock sites in eastern North America, *Bull. Seismol. Soc. Am.* **104,** 513–528.

Atkinson, G. M., and W. Silva (1997). An empirical study of earthquake source spectra for California earthquakes, *Bull. Seismol. Soc. Am.* **87,** 97–113.

Atkinson, G. M., and W. Silva (2000). Stochastic modeling of California ground motions, *Bull. Seismol. Soc. Am.* **90,** 255–274.

Atkinson, G. M., and D. J. Wald (2007). “Did You Feel It?” Intensity data: A surprisingly good measure of earthquake ground motion, *Bull. Seismol. Soc. Am.* **78,** 362–368.

Atkinson, G. M., D. M. Boore, K. Assatourians, K. Campbell, and D. Motazedian (2009). A guide to differences between stochastic point-source and stochastic finite-fault simulations, *Bull. Seismol. Soc. Am.* **99,** 3192–3201.

Baltay, A. S., and T. C. Hanks (2014). Understanding the magnitude dependence of PGA and PGV in NGA-West 2 data, *Bull. Seismol. Soc. Am.* **104,** 2851–2865.

Beresnev, I. A., and G. M. Atkinson (1997). Modeling finite-fault radiation from the ω^n spectrum, *Bull. Seismol. Soc. Am.* **87,** 67–84.

Beresnev, I. A., and G. M. Atkinson (1998). FINSIM—A FORTRAN program for simulating stochastic acceleration time histories from finite faults, *Seismol. Res. Lett.* **69,** 27–32.

Beresnev, I. A., and G. M. Atkinson (1999). Generic finite-fault model for ground motion prediction in eastern North America, *Bull. Seismol. Soc. Am.* **89,** 608–625.

Beresnev, I. A., and G. M. Atkinson (2002). Source parameters of earthquakes in eastern and western North America based on finite-fault modeling, *Bull. Seismol. Soc. Am.* **92,** 695–710.

Boatwright, J., and L. Seekins (2011). Regional spectral analysis of three moderate earthquakes in northeastern North America, *Bull. Seismol. Soc. Am.* **101,** 1769–1782.

Boore, D. M. (1983). Stochastic simulation of high-frequency ground motion based on seismological models of the radiated spectra, *Bull. Seismol. Soc. Am.* **73,** 1865–1893.

Boore, D. M. (2003). Prediction of ground motion using the stochastic method, *Pure Appl. Geophys.* **160,** 635–676.

Boore, D. M. (2005). SMSIM—Fortran programs for simulating ground motions from earthquakes: Version 2.3–A revision of OFR 96-80-A, *U.S. Geol. Surv. Open-File Rept. 2000-509*, Revised 15 August 2005, 55 pp.

Boore, D. M. (2009). Comparing stochastic point-source and finite-source ground-motion simulations: SMSIM and EXSIM, *Bull. Seismol. Soc. Am.* **99,** 3202–3216.

Boore, D. M. (2010). Orientation-independent, nongeometric-mean measures of seismic intensity from two horizontal components of motion, *Bull. Seismol. Soc. Am.* **100,** 1830–1835.

Boore, D. M. (2013). The uses and limitations of the square-root-impedance method for computing site amplification, *Bull. Seismol. Soc. Am.* **103,** 2356–2368.

Boore, D. M. (2015). Point-source stochastic-method simulations of ground motions for the PEER NGA-East project, Chapter 2 in NGA-East: Median ground-motion models for the central and eastern North America region, *PEER Report 2015/04*, Pacific Earthquake Engineering Research Center, 11–49.

Boore, D. M., and K. W. Campbell (2017). Adjusting central and eastern North America ground-motion intensity measures between sites with different reference-rock site conditions, *Bull. Seismol. Soc. Am.* **107,** 132–148.

Boore, D. M., and W. B. Joyner (1997). Site amplification for generic rock sites, *Bull. Seismol. Soc. Am.* **87,** 327–341.

Boore, D. M., and E. M. Thompson (2014). Path durations for use in the stochastic-method simulation of ground motions, *Bull. Seismol. Soc. Am.* **104,** 2541–2552.

Boore, D. M., and E. M. Thompson (2015). Revisions to some parameters used in stochastic method simulations of ground motion, *Bull. Seismol. Soc. Am.* **105,** 1029–1041.

Boore, D. M., K. W. Campbell, and G. M. Atkinson (2010). Determination of stress parameters for eight well-recorded earthquakes in eastern North America, *Bull. Seismol. Soc. Am.* **100,** 1632–1645.

Boore, D. M., J. P. Stewart, E. Seyhan, and G. M. Atkinson (2014). NGA-West2 equations for predicting PGA, PGV, and 5% damped PSA for shallow crustal earthquakes, *Earthq. Spectra* **30,** 1057–1085.

Bozorgnia, Y., N. A. Abrahamson, L. Al Atik, T. D. Ancheta, G. M. Atkinson, J. W. Baker, A. Baltay, D. M. Boore, K. W. Campbell, B. S.-J. Chiou, *et al.* (2014). NGA-West2 research project, *Earthq. Spectra* **30,** 973–987.

Brune, J. (1970). Tectonic stress and the spectra of seismic shear waves, *J. Geophys. Res.* **75,** 4997–5009.

Brune, J. (1971). Correction: Tectonic stress and the spectra of seismic shear waves, *J. Geophys. Res.* **76,** 5002.

Building Seismic Safety Council (BSSC) (2009). *NEHRP Recommended Seismic Provisions for New Buildings and Other Structures (FEMA P-75)* (2009 Edition), Building Seismic Safety Council, Washington, D.C.

Burger, R., P. Somerville, J. Barker, R. Herrmann, and D. Helmberger (1987). The effect of crustal structure on strong ground motion attenuation relations in eastern North America, *Bull. Seismol. Soc. Am.* **77,** 420–439.

Campbell, K. W. (2003). Prediction of strong ground motion using the hybrid empirical method and its use in the development of ground-motion (attenuation) relations in eastern North America, *Bull. Seismol. Soc. Am.* **93,** 1012–1033.

Campbell, K. W. (2007). *Validation and Update of Hybrid Empirical Ground Motion (Attenuation) Relations for the CEUS, Final Report to U.S. Geological Survey*, National Earthquake Hazards Reduction External Research Program, Award Number 05HQGR0032.

Campbell, K. W. (2008). Hybrid empirical ground motion model for PGA and 5% damped linear elastic response spectra from shallow crustal earthquakes in stable continental regions: Example for eastern North America, *Proc. of the 14th World Conf. on Earthquake Engineering*, Beijing, China, 12–17 October 2008, Paper Number S03–001.

Campbell, K. W. (2009). Estimates of shear-wave Q and κ_0 for unconsolidated and semiconsolidated sediments in eastern North America, *Bull. Seismol. Soc. Am.* **99,** 2365–2392.

Campbell, K. W. (2011). Ground motion simulation using the hybrid empirical method: Issues and insights, in *Earthquake Data in Engineering Seismology: Predictive Models, Data Management and Networks*, S. Akkar, P. Gulkan, and T. van Eck (Editors), Geotechnical, Geological and Earthquake Engineering Series, Vol. 14, Springer, London, United Kingdom, 81–95.

Campbell, K. W. (2014). An evaluation of eastern North America ground-motion models developed using the hybrid empirical method, *Bull. Seismol. Soc. Am.* **104,** 347–359.

Campbell, K. W., and Y. Bozorgnia (2008). NGA ground motion model for the geometric mean horizontal component of PGA, PGV, PGD and 5% damped linear-elastic response spectra for periods ranging from 0.01 to 10.0 s, *Earthq. Spectra* **24,** 139–171.

Campbell, K. W., and Y. Bozorgnia (2014). NGA-West2 ground motion model for the average horizontal components of PGA, PGV, and 5% damped linear acceleration response spectra, *Earthq. Spectra* **30,** 1087–1115.

Campbell, K. W., Y. M. A. Hashash, B. Kim, A. R. Kottke, E. M. Rathje, W. J. Silva, and J. P. Stewart (2014). Reference rock site conditions for central and eastern North America: Part II—Attenuation (kappa) definition, *PEER Report 2014/12*, Pacific Earthquake Engineering Research Center, University of California, Berkeley, California, 54 pp.

Chapman, M. C., and R. W. Godbee (2012). Modeling geometrical spreading and the relative amplitudes of vertical and horizontal high-frequency ground motions in eastern North America, *Bull. Seismol. Soc. Am.* **102,** 1957–1975.

Chapman, M., S. Pezeshk, M. Hosseini, and A. Conn (2014). Regional study of Fourier amplitude drop of *Lg*-wave acceleration in central United States, *Seismol. Res. Lett.* **85,** 513.

Chen, Y. H., and C.-C. P. Tsai (2002). A new method of estimation of the attenuation relationship with variance components, *Bull. Seismol. Soc. Am.* **92,** 1984–1991.

Chiou, B. S.-J., and R. R. Youngs (2014). Update of the Chiou and Youngs NGA model for the average horizontal component of peak ground motion and response spectra, *Earthq. Spectra* **30,** 1117–1153.

Douglas, J. (2003). Earthquake ground motion estimation using strong-motion records: A review of equations for the estimation of peak ground acceleration and response spectral ordinates, *Earth Sci. Rev.* **61,** 43–104.

Douglas, J. (2011). Ground-motion prediction equations, 1964–2010, *PEER Report 2011/102*, Pacific Earthquake Engineering Research Center, University of California, Berkeley, California, updates available online at http://www.gmpe.org.uk (last accessed November 2014).

Douglas, J., H. Bungum, and F. Scherbaum (2006). Ground-motion prediction equations for southern Spain and southern Norway obtained using the composite model perspective, *J. Earthq. Eng.* **10,** 33–72.

Dreger, D. S., G. C. Beroza, S. M. Day, C. A. Goulet, T. H. Jordan, P. A. Spudich, and J. P. Stewart (2015). Validation of the SCEC broadband platform v14.3 simulation methods using pseudospectral acceleration data, *Seismol. Res Lett.* **86,** 39–47.

Dreiling, J., M. P. Isken, W. D. Mooney, M. C. Chapman, and R. W. Godbee (2014). NGA-East regionalization report: Comparison of four crustal regions within central and eastern North America using waveform modeling and 5%-damped pseudo-spectral acceleration response, *PEER Report 2014/15*, Pacific Earthquake Engineering Research Center, University of California, Berkeley, California.

Fatehi, A., and R. B. Herrmann (2008). High-frequency ground-motion scaling in the Pacific Northwest and in northern and central California, *Bull. Seismol. Soc. Am.* **98,** 709–721.

Frankel, A., C. Mueller, T. Barnhard, D. Perkins, E. Leyendecker, N. Dickman, S. Hanson, and M. Hopper (1996). National seismic hazard maps: Documentation June 1996, *U.S. Geol. Surv. Open-File Rept. 96-532*, 110 pp.

Goulet, C. A., T. Kishida, T. D. Ancheta, C. H. Cramer, R. B. Darragh, W. J. Silva, Y. M. A. Hashash, J. Harmon, J. P. Stewart, K. E. Wooddell, *et al.* (2014). PEER NGA-East database, *PEER Report 2014/17*, Pacific Earthquake Engineering Research Center, University of California, Berkeley, California.

Graizer, V. (2016). Ground-motion prediction equations for central and eastern North America, *Bull. Seismol. Soc. Am.* **106,** 1600–1612.

Gregor, N., N. A. Abrahamson, G. M. Atkinson, D. M. Boore, Y. Bozorgnia, K. W. Campbell, B. S.-J. Chiou, I. M. Idriss, R. Kanai, E. Seyhan, *et al.* (2014). Comparison of NGA-West2 GMPEs, *Earthq. Spectra* **30,** 1179–1197.

Hanks, T. C. (1982). $f_{\max}$, *Bull. Seismol. Soc. Am.* **72,** 1867–1879.

Hanks, T. C., and R. K. McGuire (1981). The character of high-frequency strong ground motion, *Bull. Seismol. Soc. Am.* **71,** 2071–2095.

Hashash, Y. M. A., A. R. Kottke, J. P. Stewart, K. W. Campbell, B. Kim, C. Moss, S. Nikolaou, E. M. Rathje, and W. J. Silva (2014). Reference rock site condition for central and eastern North America, *Bull. Seismol. Soc. Am.* **104,** 684–701.

Hashash, Y. M. A., A. R. Kottke, J. P. Stewart, K. W. Campbell, B. Kim, E. M. Rathje, W. J. Silva, S. Nikolaou, and C. Moss (2014). Reference-rock site conditions for central and eastern North America: Part I—Velocity definition, *PEER Report 2014/11*, Pacific Earthquake Engineering Research Center, University of California, Berkeley, California, 154 pp.

Hough, S. E. (2014). Shaking from injection-induced earthquakes in the central and eastern United States, *Bull. Seismol. Soc. Am.* **104,** 2619–2626.

Idriss, I. M. (2014). An NGA-West2 empirical model for estimating the horizontal spectral values generated by shallow crustal earthquakes, *Bull. Seismol. Soc. Am.* **30,** 1155–1177.

Kottke, A. R., and E. M. Rathje (2008). Technical manual for Strata, *PEER Report 2008/10*, Pacific Earthquake Engineering Research Center, University of California, Berkeley, California.

Ktenidou, O. J., F. Cotton, N. A. Abrahamson, and J. G. Anderson (2014). Taxonomy of κ: A review of definitions and estimation approaches targeted to applications, *Seismol. Res. Lett.* **85,** 135–146.

Mahani, A. B., and G. M. Atkinson (2013). Regional differences in ground-motion amplitudes of small-to-moderate earthquakes across North America, *Bull. Seismol. Soc. Am.* **103,** 2604–2620.

Malagnini, L., K. Mayeda, R. Uhrhammer, A. Akinci, and R. B. Herrmann (2007). A regional ground-motion excitation/attenuation model for the San Francisco region, *Bull. Seismol. Soc. Am.* **97,** 843–862.

McGuire, R. K., and T. C. Hanks (1980). RMS accelerations and spectral amplitudes of strong ground motion during the San Fernando, California, earthquake, *Bull. Seismol. Soc. Am.* **70,** 1907–1919.

Motazedian, D., and G. M. Atkinson (2005). Stochastic finite-fault modeling based on a dynamic corner frequency, *Bull. Seismol. Soc. Am.* **95,** 995–1010.

Ou, G., and R. Herrmann (1990). A statistical model for peak ground motion from local to regional distances, *Bull. Seismol. Soc. Am.* **80,** 1397–1417.

Pacific Earthquake Engineering Research Center (PEER) (2015). NGA-East: Adjustments to median ground-motion models for central and eastern North America, *PEER Report 2015/08*, Pacific Earthquake Engineering Research Center, University of California, Berkeley, California.

Petersen, M. D., A. D. Frankel, S. C. Harmsen, C. S. Mueller, K. M. Haller, R. L. Wheeler, R. L. Wesson, Y. Zeng, O. S. Boyd, D. M. Perkins, *et al.* (2008). Documentation for the 2008 update of the United States National seismic hazard maps, *U.S. Geol. Surv. Open-File Rept. 2008–1128*, 61 pp.

Petersen, M. D., M. P. Moschetti, P. M. Powers, C. S. Mueller, K. M. Haller, A. D. Frankel, Y. Zeng, S. Rezaeian, S. C. Harmsen, O. S. Boyd, *et al.* (2014). Documentation for the 2014 update of the United States national seismic hazard maps, *U.S. Geol. Surv. Open-File Rept. 2014-1091*, 243 pp.

Pezeshk, S., A. Zandieh, K. W. Campbell, and B. Tavakoli (2015). Ground motion prediction equations for eastern North America using the hybrid empirical method and NGA-West2 empirical ground motion models, Chapter 5, *PEER Report 2015/04—NGA-East: Median Ground-Motion Models for the Central and Eastern North America*, Pacific Earthquake Engineering Research Center, University of California, Berkeley, California.

Pezeshk, S., A. Zandieh, and B. Tavakoli (2011). Hybrid empirical ground-motion prediction equations for eastern North America using NGA models and updated seismological parameters, *Bull. Seismol. Soc. Am.* **101,** 1859–1870.

Power, M., B. Chiou, N. Abrahamson, Y. Bozorgnia, T. Shantz, and C. Roblee (2008). An overview of the NGA project, *Earthq. Spectra* **24,** 3–21.

Raoof, M., R. Herrmann, and L. Malagnini (1999). Attenuation and excitation of three-component ground motion in southern California, *Bull. Seismol. Soc. Am.* **89,** 888–902.

Rodriguez-Marek, A., F. Cotton, N. A. Abrahamson, S. Akkar, L. Al Atik, B. Edwards, G. A. Montalva, and H. M. Dawood (2013). A model for single-station standard deviation using data from various tectonic regions, *Bull. Seismol. Soc. Am.* **103,** 3149–3163.

Scherbaum, F., J. J. Bommer, H. Bungum, F. Cotton, and N. A. Abrahamson (2005). Composite ground-motion models and logic trees: Methodology, sensitivities, and uncertainties, *Bull. Seismol. Soc. Am.* **95,** 1575–1593.

Scherbaum, F., F. Cotton, and H. Staektke (2006). The estimation of minimum-misfit stochastic model from empirical ground-motion prediction equations, *Bull. Seismol. Soc. Am.* **96,** 417–445.

Scherbaum, F., J. Schmedes, and F. Cotton (2004). On the conversion of source-to-site distance measures for extended earthquake source models. *Bull. Seismol. Soc. Am.* **94,** 1053–1069.

Shahjouei, A., and S. Pezeshk (2016). Alternative hybrid empirical ground motion prediction equations for central and eastern North America using hybrid simulations and NGA-West2 models, *Bull. Seismol. Soc. Am.* **106,** 737–754.

Silva, W., N. Gregor, and R. Darragh (2002). Development of regional hard rock attenuation relations for central and eastern North America, *Technical Report*, Pacific Engineering & Analysis, El Cerrito, California, 57 pp.

Silva, W. J., R. B. Darragh, C. Stark, I. Wong, J. C. Stepp, J. Schneider, and B. S.-J. Chou (1990). A methodology to estimate design response spectra in the near-source region of large earthquakes using the band-limited-white-noise ground motion model, *Proc. of the 4th U.S. National Conf. on Earthquake Engineering*, Vol. 1, Palm Springs, California, 20–24 May 1990, *U.S. Geol. Surv. Open-File Rept. 89-465*, 487–494.

Somerville, P., N. Collins, N. Abrahamson, R. Graves, and C. Saikia (2001). *Ground Motion Attenuation Relations for the Central and Eastern*

United States, Final Report to U.S. Geological Survey, National Earthquake Hazards Reduction External Research Program, Award Number 99HQGR0098.

Somerville, P., R. Graves, N. Collins, S.-G. Song, S. Ni, and P. Cummins (2009). Source and ground motion models for Australian earthquakes, *Proc. of the 2009 Australian Earthquake Engineering Society Conf.*, Newcastle, Australia, 11–13 December 2009.

Tavakoli, B., and S. Pezeshk (2005). Empirical-stochastic ground-motion prediction for eastern North America, *Bull. Seismol. Soc. Am.* **95,** 2283–2296.

Toro, G. R., N. A. Abrahamson, and J. F. Schneider (1997). Model of strong ground motions from earthquakes in central and eastern North America: Best estimates and uncertainties, *Seismol. Res. Lett.* **68,** 41–57.

Yenier, E., and G. M. Atkinson (2014). Equivalent point-source modeling of moderate to large magnitude earthquakes and associated ground-motion saturation effects, *Bull. Seismol. Soc. Am.* **104,** 1458–1478.

Yenier, E., and G. M. Atkinson (2015a). Regionally adjustable generic ground-motion prediction equation based on equivalent point-source simulations: Application to central and eastern North America, *Bull. Seismol. Soc. Am.* **105,** 1989–2009.

Yenier, E., and G. M. Atkinson (2015b). An equivalent point-source model for stochastic simulation of earthquake ground motions in California, *Bull. Seismol. Soc. Am.* **105,** 1435–1455.

Youngs, R. R., and N. Kuehn (2015). Extension of median ground-motion models to short and large distances, Chapter 2, *PEER Report 2015/08 —NGA-East Adjustments to Median Ground-Motion Models for Central And Eastern North America*, Pacific Earthquake Engineering Research Center, University of California, Berkeley, California.

Zandieh, A., K. W. Campbell, and S. Pezeshk (2016). Estimation of κ_0 implied by the high-frequency shape of the NGA-West2 ground-motion prediction equations, *Bull. Seismol. Soc. Am.* **106,** 1342–1356.

Department of Civil Engineering
The University of Memphis
104 Engineering Science Building
Memphis, Tennessee 38152
spezeshk@memphis.edu
(S.P.)

Lettis Consultants International, Inc. (LCI)
4155 Darley Avenue, Suite A
Boulder, Colorado 80305
(A.Z.)

CoreLogic Inc.
555 12th Street, Suite 1100
Oakland, California 94612
(K.W.C.)

Department of Seismology and Geophysics
G&HES, Bechtel Corporation
50 Beale Street
San Francisco, California 94105
(B.T.)

Manuscript received 21 June 2017;
Published Online 19 June 2018